Journal of Physics D:
Applied Physics

Solvent-free manufacturing and 3D printing of ceramic-rich biopolymeric PHA-based piezocomposite for eco-friendly mechanical sensors

To cite this article: Malik Daniyal Zaheer *et al* 2025 *J. Phys. D: Appl. Phys.* **58** 475501

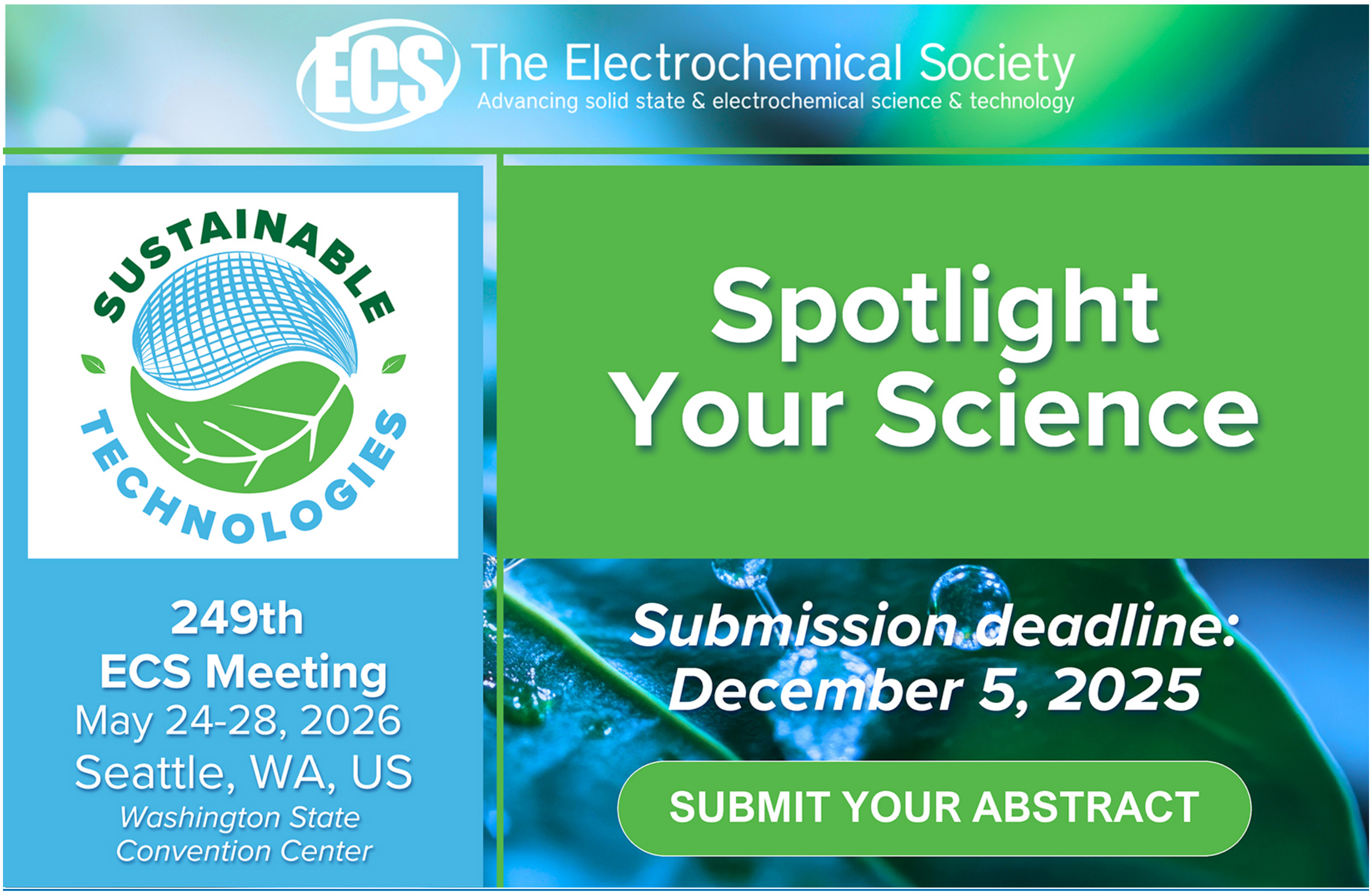

OPEN ACCESS
IOP Publishing
Journal of Physics D: Applied Physics
J. Phys. D: Appl. Phys. **58** (2025) 475501 (18pp)
https://doi.org/10.1088/1361-6463/ae1d8b

Solvent-free manufacturing and 3D printing of ceramic-rich biopolymeric PHA-based piezocomposite for eco-friendly mechanical sensors

Malik Daniyal Zaheer[1], **Rolanas Dauksevicius**[1,*], **Qasim Zia**[2] and **Madeeha Tabassum**[3]

[1] Institute of Mechatronics, Kaunas University of Technology, Studentu str. 56, 51424 Kaunas, Lithuania
[2] School of Engineering and Materials Science, Queen Mary University of London, NanoVision Centre, E14NS London, United Kingdom
[3] Materials and Engineering Research Institute, Sheffield Hallam University, S11WB Sheffield, United Kingdom

E-mail: rolanas.dauksevicius@ktu.lt

Received 25 August 2025, revised 30 October 2025
Accepted for publication 10 November 2025
Published 20 November 2025

Abstract

Similarly to the developments in green electronics, the emerging field of additive piezo-electronics increasingly focuses on more sustainable electroactive materials and cleaner production workflows. However, solution processing with hazardous solvents remains common, even for hybrid organic-inorganic piezoelectric materials (piezocomposites) made from eco-friendly biopolyesters polyhydroxyalkanoates, including ductile copolymer poly(3-hydroxybutyrate-co-3-hydroxyhexanoate)(PHBHHx). Therefore, we investigated the solvent-free extrusion-based manufacturing and fused filament fabrication (FFF) of lead-free piezoceramic-rich PHBHHx composite with 80 wt% of barium titanate (BTO). Physicochemical characterization of filaments and prints revealed favorable melt reprocessing capability of PHBHHx as both neat and BTO-rich biopolymers retained chemical structure and thermal stability after three remelting cycles (single or double extrusion at 130 °C–140 °C and FFF at 170 °C). The re-extrusion and FFF processes were calibrated to ensure consistent printability of well-homogenized and well-fused piezocomposite (0–3 connectivity). The tensile loading of neat and BTO-rich PHBHHx structures at increasing speeds revealed complex material behavior of strain-rate-dependent strengthening, weakening, hardening and softening. Despite the high BTO fraction, the composite maintained acceptable flexibility, although the tensile strength decreased due to weaker filler-matrix interfacial bonding. The piezoelectric response and stabilization (d_{33} decay due to initial ferroelectric depolarization) were analyzed over a wide range of poling fields and durations. The 3D-printed piezocomposite demonstrated

---

[*] Author to whom any correspondence should be addressed.

excellent high-field poling capability up to ~22 kV mm^{-1}. It provided a comparatively high maximum piezoresponse of ~11 pC/N, matching the predictions of the Jayasundere–Smith model for two-phase particulate composites. The presented sustainable and scalable melt-based workflow is accessible to the 3D printing community, supporting democratization and further advances in the material extrusion additive manufacturing of piezoelectric sensors, energy harvesters/nanogenerators and other devices. The experimental findings are useful for the development of environmentally safe melt processing routes to produce highly filled PHBHHx-based composites.

Supplementary material for this article is available online

Keywords: biodegradable bioplastic, compostable PHBH, P(3HB-co-3HHx), polymer-ceramic composite, nanocomposite, FDM, electromechanical response

1. Introduction

In pursuit of reducing e-waste and developing environmentally safe smart systems, green electronics has become a rapidly growing research field, covering diverse 2D or 3D printing technologies [1, 2]. It also includes additive manufacturing (AM) of piezoelectric sensors, nanogenerators and other devices (piezo-devices) for industrial, environmental, and biomedical uses [3, 4]. Further progress in printed greener electroactive materials (e.g. lead-free and halogen-free) is essential for advancing more sustainable piezo-electronics. In particular, 3D-printable biopolymeric piezocomposites provide a versatile and eco-friendly material platform for tuning electromechanical properties to optimize piezo-devices for specific application requirements [5, 6].

The biosynthesized polyhydroxyalkanoates (PHAs) emerged as promising biopolymers for the AM of eco-friendly multifunctional products [7]. Natural biodegradability of PHAs (in soil, water, home compost) [8] makes them a superior alternative to conventional biodegradable polyesters, which are typically fossil-based or only partially bio-based (e.g. PCL, PBAT, PBS), or are fully bio-based but limited to industrial composting (e.g. PLA). The short-chain length grades (scl-PHAs) have been widely studied, particularly the brittle poly(3-hydroxybutyrate) (P3HB/PHB) and the less rigid copolymers with 3-hydroxyvalerate 3HV (PHBV). However, their narrow thermal processing window complicates melt-based manufacturing such as material extrusion (MEX) AM using fused filament fabrication (FFF). Therefore, more ductile medium-chain length grades (mcl-PHAs) [9] are actively developed worldwide. Mechanical performance of (piezo)composites with hard fillers may largely benefit from the elastomer-like properties of mcl-PHA matrix [10], including PHB copolymer with 3-hydroxyhexanoate 3HHx (PHBHHx) that may exhibit elongations of tens or even hundreds of percent [8]. It offers an improved melt processability as the effective temperature window increases with higher 3HHx content [9]. Earlier research on melt-processed (e.g. extruded) PHBHHx-based materials was mostly limited to Kaneka grades [11–14], though grades from other producers were tested recently (e.g. Ercros [15, 16], Panara [17] and Bluepha [18]).

Diverse ceramic and carbonaceous fillers are added to modify the material properties and impart PHA composites with useful functions such as antibacterial, thermal and electrical ones [19], including the piezoelectric effect. We note that filler content in the PHA piezocomposites is typically less than 50 wt% (table S1). It mitigates brittleness when using rigid scl-PHAs, but reduces the maximum achievable piezoresponse, which strongly depends on the active filler fraction [20]. Prior studies on piezoelectric PHA-based materials are not abundant (table S1). Neat PHAs are organic piezoelectric materials [21] that exhibit weak shear piezoresponse (~1–2 pC/N for stretched scl-PHA films [22] and <1 pC/N for molded mcl-PHA films [23]). Longitudinal and transverse piezoresponses were detected in the fibrous electrospun PHB ($d_{33} \approx$ 2.1–5.0 pC/N) [24–28], $d_{31} \approx$ 4.1 pC/N [24]). Ferroelectric and pyroelectric behavior was observed in PHAs as well [29]. The piezocomposites were fabricated using mostly scl-PHAs paired with piezoceramics, including ferroelectric lead-based [30] or lead-free compositions (e.g. BTO [31–35], KNN [36]), and non-ferroelectric fillers (e.g. ZnO [25], hydroxyapatite [37]). There is a severe lack of research on using more ductile mcl-PHAs in piezocomposites (possibly a single study to date [33]). BTO is a very common choice due to its moderate cost, wide availability and applicability. Due to potential biocompatibility the BTO [38] and PHAs [21] are considered as candidate materials for implanted devices. In some studies conductive modifiers were added to enhance piezoresponse (e.g. carbonaceous nanomaterials [39–41] or conducting polymers [42]). The piezoresponse was typically evaluated by measuring d_{33} using a quasi-static meter (table S1), though d_{33} was not always reported [34, 36, 43]. Piezoresponse optimization via tuning of poling conditions is very important for developing functional devices. However, earlier studies were often limited in scope by testing either a single poling field [33–35] or duration [33–36].

PHA-based piezoelectric materials were mostly fabricated using solvent-based methods (table S1). Many studies adopted electrospinning of neat scl-PHAs [27, 28], blends with other polymers [26, 42], and composites with piezoceramics [25, 32, 37] or carbonaceous nanomaterials [39–41]. Solution casting [22, 34, 36], DIW-printing [43] and particulate leaching [35] were also applied. Despite the known health and environmental risks [44], most reported workflows relied on hazardous solvents [45], predominantly chloroform that was used widely in electrospinning (table S1). PHAs were also processed with other hazardous solvents, including DCM [34], HFIP [36] and even substances of very high concern such as highly toxic polar aprotic solvents [46] (e.g. DMF [35, 42]). Such solvent-based approaches are environmentally unsound and represent a contradiction in sustainability because toxic solvents are employed in the manufacturing of composites meant to be sustainable due to the use of eco-friendly PHAs. Moreover, solution processing poses limitations in the design freedom of PHA products and presents obstacles for industrial production. Solution casting, which consumes large amounts of solvents, may complicate the production of geometrically intricate monolithic piezo-devices composed of integrated piezoelectric, conductive and insulating layers. Meanwhile, conventional electrospinning mainly produces fibrous structures of relatively simple shapes and, in contrast to AM, may be less suited for the single-process manufacturing of monolithic multilayer piezo-devices of intricate shapes [4].

The solvent-free fabrication was rarely used for PHA-based piezoelectric materials (table S1) and was performed by molding [23, 30] or extrusion [31]. Filler homogenization in the PHA piezocomposites was accomplished using dry mixing [30] or specialized melt compounders (e.g. Brabender mixer [31]). Filler dispersion uniformity is essential for consistent composite properties as poorly dispersed filler particles may create micropores and agglomerations. In piezocomposites, such defects lead to reduced toughness and inferior polarization of a ferroelectric filler (weaker piezoresponse is induced because structural inhomogeneities cause uneven electrical field distribution during poling [20]).

We emphasize that studies on FFF of PHA piezocomposites are extremely scarce, with only a single report to our knowledge (PHB was 3D printed with low BTO content of 20 wt% [31]). This lack of studies aligns with the broader research landscape since the 3D printing of fully bio-based multifunctional PHA products without petrochemical polymer blends is still in its early stages [47]. Research on 3D printed PHAs (particularly PHBHHx) is limited compared to competing biopolyesters such as PLA [48]. Nevertheless, FFF of various (non-piezoelectric) PHBHHx-based materials has recently started to gain momentum, demonstrating wider adoption of solvent-free processes [15, 49–52] or hybrid melt/solvent-based workflows to minimize solvent use for easier industrial upscaling [53].

In this study, we address major limitations of less sustainable manufacturing and suboptimal piezoelectric performance of the reported PHA piezocomposites, which were mostly produced by non-AM methods with hazardous solvents and (semi)brittle scl-PHAs at low ceramic content, resulting in limited piezoresponse. Furthermore, the effects of rapid high-field poling and the initial post-poling d_{33} decay have not been investigated, even though efficient poling and stable piezoresponse are crucial for practical devices. The study contributes to the field of additive piezo-electronics by pursuing a cleaner production route and tackling the underexplored challenges of scalable solvent-free manufacturing, FFF-printing, high-field poling, and d_{33} enhancement of highly filled PHA piezocomposites. We demonstrate an economical melt-based workflow to produce well-homogenized and sufficiently flexible ceramic-rich PHBHHx piezocomposite with the maximum printable BTO content of 80 wt%, enabling consistent high-field poling and maximized d_{33}. The approach follows safe-and-sustainable-by-design principles, avoiding hazardous solvents and additives to ensure environmental safety. Single- and double-extruded filaments of neat and BTO-rich PHBHHx were printed and tested to evaluate the influence of re-extrusion on the thermal, morphological, and mechanical properties. A detailed piezoelectric analysis was performed to determine how d_{33} and its stabilization are affected by the wide-ranging poling fields and durations. The results provide valuable insights for effective melt-based manufacturing of PHBHHx-based (piezo)composites with densely packed hard fillers.

2. Extrusion and 3D printing of PHBHHx-based filaments

2.1. Materials

The fully biobased, water/soil-degradable and home-compostable semi-crystalline PHBHHx Bluepha® BP350-15 powder (Bluepha Co., Ltd (China)) has 10 mol% HHx, melting point of 133 °C, glass transition temperature of −2 °C, density of 1.19 g cm^{-3} and MFI of 10–15 g 10 min^{-1} (165 °C, 5 kg) [18]. Submicron-sized BTO particles (Inframat Advanced Materials LLC (USA)) have a density of 5.85 g cm^{-3} with a nominal average particle diameter of 0.5 μm.

2.2. Extrusion of neat and BTO-rich PHBHHx filaments

The PHBHHx powder was dried in oven Memmert UFB 400 at 65 °C for 6 h to eliminate residual moisture. The dried powder was extruded into PHBHHx filament batch (single-extruded filament F1 in table 1). Some of the filament was pelletized and re-extruded to produce the double-extruded filament F2 (figure 1(b)). Piezocomposite filaments of PHBHHx/BTO were manufactured through a dry processing route using double-extrusion workflow to achieve more uniform filler dispersion (figure 1(a)). The workflow started with the preparation of the composite premix by tumble blending powders of PHBHHx and BTO (20/80 wt%). The premix was extruded into an intermediate filament (F1-BTO80), part of which was pelletized and re-extruded into the final filament (F2-BTO80). The filaments were printed to produce single- and double-extruded prints (P1-BTO80 and P2-BTO80, respectively in table 1). The extrusion was performed using a conventional single-screw extruder Noztek Touch equipped with two heating zones and a ⌀1.75 mm nozzle. An acceptable dimensional

Table 1. Labeling of extruded and printed samples.

Label	Description
F*i*	PHBHHx filaments extruded $i = 1 - 2$ times (i.e. single- and double-extruded samples).
F*i*-BTO80	20/80 wt% PHBHHx/BTO piezocomposite filaments extruded $i = 1 - 2$ times.
P*i*	PHBHHx samples printed with single- or double-extruded filaments.
P*i*-BTO80	20/80 wt% PHBHHx/BTO printed with single- or double-extruded filaments.
P*i*-BTO80-P	Printed and poled 20/80 wt% PHBHHx/BTO piezocomposite samples.

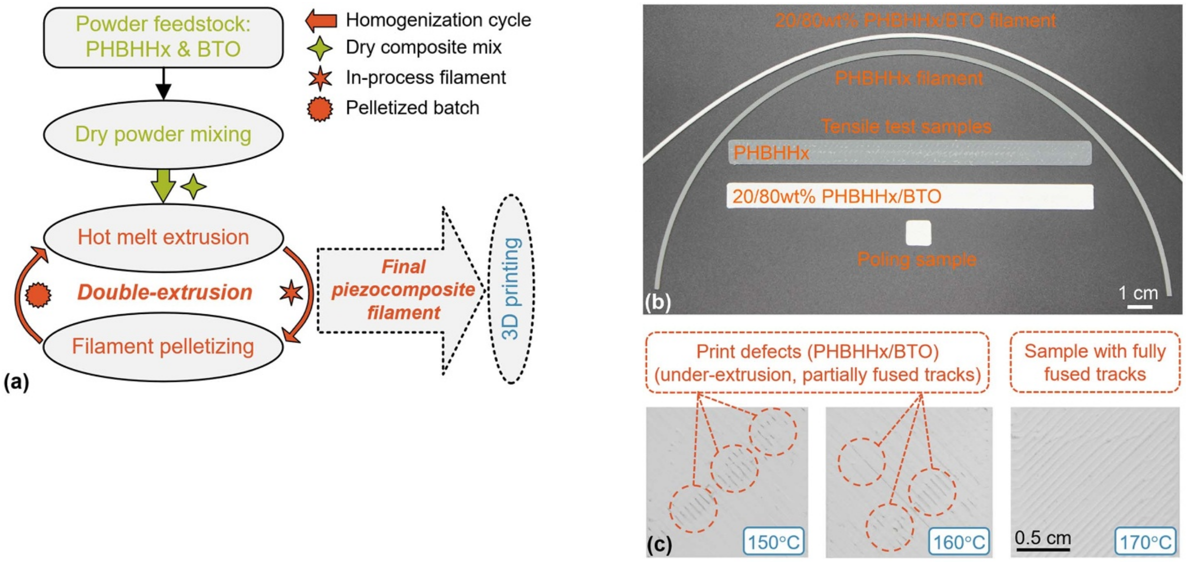

Figure 1. (a) Double-extrusion workflow for solvent-free fabrication of 20/80 wt% PHBHHx/BTO filaments. (b) Extruded filaments and 3D prints of PHBHHx-based materials. (c) Quality of the piezocomposite printed at different temperatures.

accuracy of the filaments ($\varnothing 1.75 \pm 0.05$ mm) was achieved by installing the extruder at 45° for the filament to be freely tensioned by gravity. A simple in-house pelletizer was built to cut the filaments into small pellets.

When applying re-extrusion for piezocomposite manufacturing, it was important to mitigate the risk of PHBHHx decomposition (its thermal stability is comparable to PLA [12]). Therefore, multiple extrusion trials were performed using different barrel and nozzle temperatures arranged in either the forward or reverse heating profiles. The objective was to produce filaments of consistent quality while attempting to reduce the extrusion temperatures and minimize the risk of thermal degradation. It was determined that a forward heating profile in the vicinity of PHBHHx melting point delivered effective extrusion of neat and BTO-rich filaments (barrel and nozzle zones were set to 130 °C and 140 °C, respectively). A slightly higher temperature in the nozzle zone was required to ensure a stable melt flow rate and maintain a proper thermal balance at the nozzle (forced air cooling was not applied). The forward heating profile close to the melting point was also preferred in other studies [11, 54]. The extruder motor was run at a relatively low speed of 18 RPM, which ensured stable extrusion of high-quality filaments of consistent diameter. It also provided a more uniform BTO dispersion within the PHBHHx matrix, which provided a better surface finish for the piezocomposite filament.

2.3. FFF of test samples

The experimental samples (figure 1(b)) were printed with the single- and double-extruded filaments in FFF machine Prusa i3 MK3S+ using PrusaSlicer 3.14.1. We note that PHBHHx in the double-extruded prints P2 and P2-BTO80 (table 1) was remelted three times in total.

The piezocomposite filament exerts an abrasive effect on the nozzle as nearly half of its volume is composed of hard particles (∼45 vol% BTO). Therefore, the printer was equipped with a wear-resistant vanadium-alloyed steel nozzle ($\varnothing 0.8$ mm). This facilitated printing by reducing nozzle clogging, maintaining a stable nozzle temperature, and enabling consistent deposition of the highly filled piezocomposite melt. Table 2 lists the most effective FFF settings established through iterative printing trials. They allowed the fabrication of well-fused samples with consistent mechanical properties and high breakdown strength ($\geqslant 22$ kV mm^{-1}) for superior poling stability needed to maximize the piezoresponses (sections 3.2 and 3.3).

A high ceramic content in the filament reduces the flowability and can result in a non-homogeneous melt with local BTO agglomerations, which may hinder or even block the flow in the nozzle. Intermittent melt flow, subpar interlayer fusion and visible print surface defects were observed during piezocomposite printing trials at lower temperatures of 150 °C–160 °C (i.e. ∼20 °C–30 °C above the specified

Table 2. Summary of 3D printing settings.

Parameters	Description
Nozzle diameter (material)	0.8 mm (vanadium steel)
Nozzle/print bed temperature	170 °C/70 °C
Print bed surface (adhesive coat)	Smooth PEI (Dimafix®)
Printing speed (fan operation)	10 mm s^{-1} (fan off)
Extrusion multiplier	1.2
Extrusion width, layer height	0.9 mm, 0.15 mm
Infill pattern (density, rastering)	Rectilinear (100%, ±45°)
FFF duration: tensile, poling sample	~14 min, ~5 min

melting temperature of Bluepha® BP350-15)(figure 1(c)). Therefore, to reduce piezocomposite melt viscosity, the printing temperature was increased to 170 °C. This prevented intermittent flow and mitigated nozzle clogging risks, which enabled continuous and uniform melt deposition, resulting in dimensionally stable prints with the well-fused layers. FFF trials revealed that neat PHBHHx filaments could be successfully printed at a lower temperature of ~150 °C. However, a single printing temperature of 170 °C was used for all samples to allow for a meaningful comparison between the material properties of the neat and BTO-rich PHBHHx (i.e. fabricated under identical extrusion and printing conditions). To ensure better adhesion of the first print layer and prevent warping, Dimafix® adhesive spray was applied to the print bed (heated to 70 °C). All samples were printed flat at 10 mm s^{-1} using 100% rectilinear infill. An extrusion multiplier of 1.2 was applied to prevent under-extrusion and formation of interlayer voids with surface irregularities. The samples were composed of three layers (nominal thickness of 0.15 mm) with a total measured thickness of ~0.55 mm due to higher extrusion multiplier.

Compared to PLA, the printing of PHA requires more careful control of FFF conditions because of the more complex semi-crystalline structure [19]. This can easily cause non-uniform shrinkage, warping and poor bed adhesion, particularly in open-chamber 3D printers with a less stable thermal environment. We observed that the PHBHHx samples were prone to warping when the cooling process was excessively rapid (e.g. if the print bed was unheated or if the solidification was accelerated by the airflow from the printer fan). FFF experiments demonstrated that a heated bed with a deactivated fan provided strong first-layer adhesion and effectively controlled the crystallization behavior, which enabled the uninterrupted printing of warp-free samples. Moreover, PHAs exhibit a relatively slow crystallization rate [8, 9, 19], which complicates the FFF workflow. Both neat and BTO-rich PHBHHx samples exhibited lower strength and higher flexibility if removed from the bed immediately after printing, implying incomplete crystallization process. Therefore, to ensure complete solidification of PHBHHx and maintain dimensional stability, the samples were left on the print bed to cool to room temperature. A 20 min period of slow unforced cooling was sufficient to allow for more uniform crystallization of the deposited layers, which improved interlayer fusion and resulted in stronger prints.

2.4. *Tensile testing*

Quasistatic tensile tests were conducted with UTM Tinius Olsen H25KT (figure 2(a)) by using printed thin strips (figure 1(b)) of 150 × 10 × 0.55 mm^3 (Type 2 samples in ISO 527–3). They were clamped in wedge-action grips (100 mm distance) and tested at 10, 100, and 1000 mm min^{-1} (i.e. low strain rate regime [55] of 0.0017, 0.017 and 0.17 s^{-1}, respectively). Five samples were printed to assess the average tensile strength and modulus along with the yield and fracture strains. A video extensometer Tinius Olsen VEM300 was used to measure the strains by recording the displacement between two sets of gauge marks over a 50 mm gauge length. Tensile strength was calculated as the ratio of the maximum force recorded at the first peak to the initial cross-sectional area. The tensile modulus was evaluated as the slope of the secant line between the strains of $\varepsilon_1 = 0.0005$ and $\varepsilon_2 = 0.0025$, using the ratio $(\sigma_2 - \sigma_1)/(\varepsilon_2 - \varepsilon_1)$, where σ_1 and σ_2 represent the corresponding stress values.

2.5. *Electrical poling and piezoresponse measurements*

The printed piezocomposite sheets (10 × 10 × 0.55 mm^3) were covered with 50 μm copper foil for poling in silicone oil at 60 °C (the temperature was found to be efficient for maximizing d_{33} [56]). High-voltage amplifier Spellman SL600 was used to apply DC fields of ~3.6–22.5 kV mm^{-1} over 2–2000 s (figure 2(b)). The d_{33} was measured using a Berlincourt-type meter PolyK PKD3-2000-F10N with a force-sensing unit. The samples were preloaded with 4 N and then compressed with 0.25 N at 110 Hz (three samples were tested for each poling case). The initial post-poling decay of d_{33} values was monitored over the next two days to evaluate the short-term depolarization. The first value was recorded ~2 min after poling, followed by measurements at 0.3, 2.8, 28 and 56 h. The d_{33} stabilized between 28 h and 56 h and showed no measurable decay over the following days. The values measured after 56 h were considered as the final stable piezoresponses.

2.6. *Physicochemical analysis*

Calorimetric measurements were conducted with TA Instruments DSC 25 to evaluate the thermal behavior of extruded filaments and printed samples, as well as to determine the effective melt processing temperatures. Samples of 5–7 mg were tested under a nitrogen atmosphere (60 ml min^{-1}). Heating and cooling rates of 20 °C min^{-1} were maintained during both the first and second DSC runs. First, the samples were heated from an ambient temperature up to 190 °C to remove any prior thermal history, followed by cooling to −50 °C, and an isothermal hold of 2 min at the end. In the second run, the samples were reheated from −50 °C to 190 °C and subsequently cooled to ambient temperature. Both the first

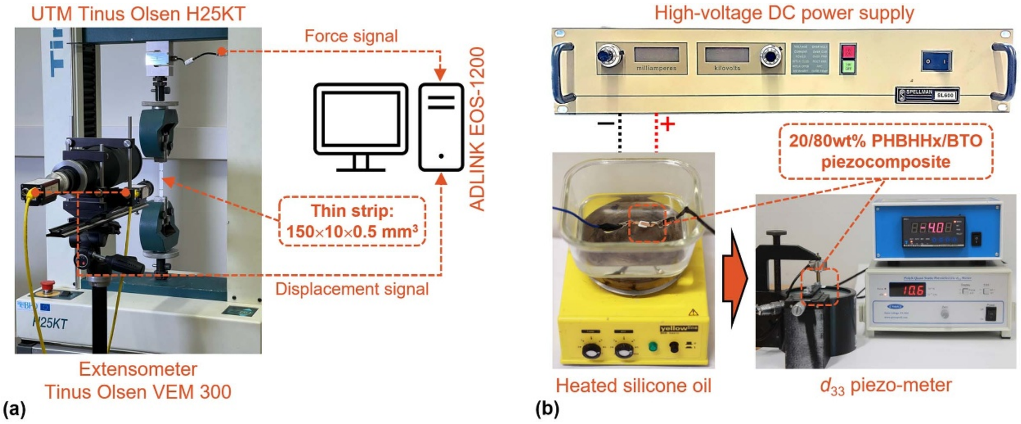

Figure 2. (a) Setup for tensile testing of 3D printed thin strip samples. (b) Devices for electrical poling and d_{33} measurement.

and second heating runs were used to calculate the melting enthalpy (ΔH_m) and temperature corresponding to the melting peak (T_m), while the glass transition temperature (T_g) was identified at the inflection point of the second heating flow curve. The degree of crystallinity (X_c) was derived as:

$$X_c = \frac{\Delta H_m}{\Delta H_{m,100\%} \times w_p} \times 100 \quad (1)$$

where ΔH_m—measured melting enthalpy, $\Delta H_{m,100\%}$—theoretical melting enthalpy for the 100% crystalline PHBHHx (115 J g^{-1} is a reasonable approximation as it is the value for the case of 8 mol% 3HHx [57], and there is 10 mol% HHx in Bluepha® BP350-15 [18]), w_p—weight fraction of the polymer.

The thermal degradation temperature and effective solid residues were determined using thermogravimetric analysis (TGA) with TA Instruments Discovery TGA 5500. Samples (10 ± 0.5 mg) were heated from 30 °C to 600 °C in 100 μl Pt sample crucible at 10 °C min^{-1} rate under N_2 flow of 20 ml min^{-1}. Thermal stability was assessed by normalizing the mass loss to the initial dehumidified mass (W_o) prior to heating and presenting the results with respect to the temperature T (°C).

The crystallographic structure and phase composition of all samples were analyzed using a Malvern Panalytical Empyrean diffractometer equipped with a copper x-ray tube (Cu-Kα radiation: Kα1 = 1.5405980 Å, Kα2 = 1.5444260 Å, and Kβ = 1.3922499 Å) operated at maximum output (voltage of 45 kV, current of 40 mA). A scan axis of 2θ was used to acquire diffraction patterns between 5° and 70° under a Bragg–Brentano reflection configuration at a scan step of 0.005°.

FTIR spectroscopy was performed to determine the chemical functional groups in all the samples using a Bruker spectrometer equipped with a universal attenuated total reflectance sampling accessory (diamond crystal). Spectra were recorded at ambient temperature by averaging 60 scans per sample, using a spectral resolution of 4 cm^{-1} over the wavenumber range of 400–4000 cm^{-1}.

The morphology of the fracture surface of the ruptured tensile samples was examined using FEI Inspect™ F SEM instrument operated at accelerated voltage of 10 kV. To enhance the image quality and prevent electrostatic charging during electron irradiation, a 10 nm gold layer was deposited on the samples before SEM analysis using an Agar Scientific manual sputter coater (model AGB7340).

3. Experimental results and discussion

3.1. Thermal and morphological properties

TGA results reveal a relatively narrow thermal decomposition window of ∼250 °C–290 °C (table 3) for the single- and double-extruded neat and BTO-rich PHBHHx filaments and prints (figure 3). All PHBHHx samples demonstrate comparable thermal stability and exhibit single-step degradation process, which starts at temperatures of $T_{d(o)}$ = 253 °C–271 °C (higher by at least ∼110 °C and ∼80 °C than the filament extrusion and 3D printing temperatures, respectively). Similar decomposition temperatures for Bluepha® PHBHHx have also been reported previously [18, 58].

Interestingly, the triple-remelted P2 sample (double-extruded and printed) decomposes at slightly higher temperatures than the single- and double-remelted samples. This suggests that the double-extrusion process executed at 130 °C–140 °C temperatures (near the PHBHHx melting point) and the subsequent 3D printing at moderately elevated temperature of 170 °C did not cause noticeable PHBHHx degradation. This is also illustrated by the comparable mechanical properties of the P1 and P2 samples (section 3.2). TGA shows that the residual mass of the PHBHHx samples is consistent ($m_f \leqslant 1\%$), and the maximum degradation rate R_{max} varies between 4.3%–5.8%/°C.

Maximum degradation rate of the piezocomposite samples is slightly lower (1.7%–2.4%/°C), which suggests more gradual thermal decomposition. However, BTO particles cause a mild degradation promoting effect as the piezocomposite samples decompose at slightly lower temperatures of $T_{d(o)}$ = 241 °C–249 °C compared to the neat PHBHHx (such finding was also reported in earlier study [31]). As expected, the ceramic filler does not decompose during TGA, and

Table 3. Thermal degradation properties of single- and double-extruded PHBHHx and 20/80 wt% PHBHHx/BTO piezocomposite filaments (F1 and F2; F1-BTO80 and F2-BTO80) and printed samples (P1 and P2; P1-BTO80 and P2-BTO80): temperatures of the degradation onset $T_{d(o)}$, peak $T_{d(p)}$ and endset $T_{d(e)}$, 5% mass loss temperature T_5, maximum degradation rate R_{max}, mass loss Δm, final mass m_f.

Sample	$T_{d(o)}$ (°C)	$T_{d(p)}$ (°C)	$T_{d(e)}$ (°C)	T_5 (°C)	R_{max} (%/°C)	Δm (%)	m_f (%)
F1	264	282	290	254	4.9	99.4	0.6
F2	265	282	288	253	5.4	99.8	0.2
P1	253	271	280	245	4.3	99.0	1.0
P2	271	286	293	262	5.8	99.2	0.8
F1-BTO80	249	258	262	250	2.4	20.2	79.8
F2-BTO80	241	253	258	244	1.7	20.1	79.9
P1-BTO80	244	257	261	246	1.7	20.5	79.5
P2-BTO80	244	255	259	245	1.8	20.4	79.6

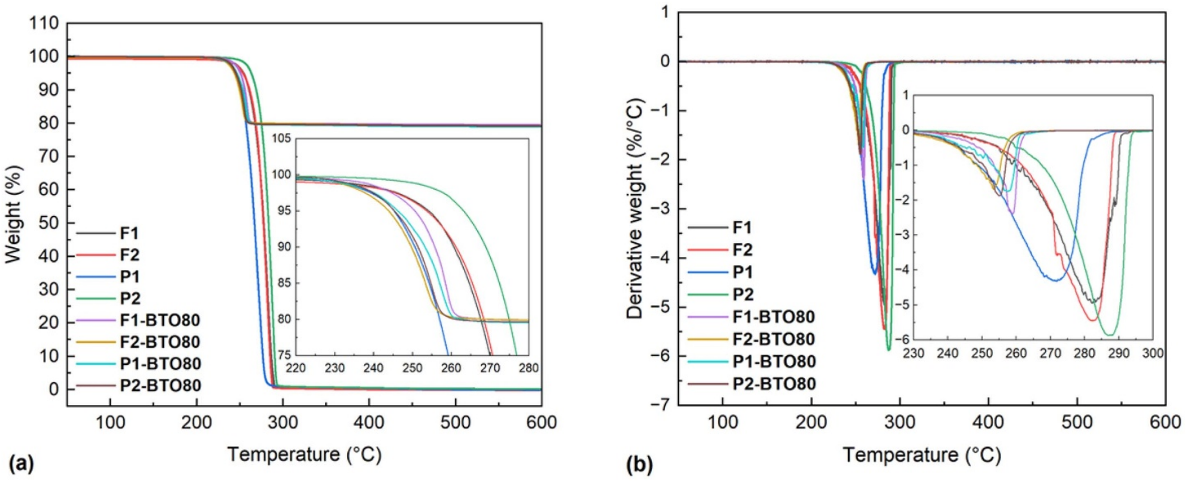

Figure 3. (a) Thermogravimetric and (b) derivative thermogravimetric curves for the single- and double-extruded PHBHHx and 20/80 wt% PHBHHx/BTO piezocomposite filaments (F*i*, F*i*-BTO80) and prints (P*i*, P*i*-BTO80).

the residual mass of the piezocomposite settles at $m_f \approx 80\%$. Overall, TGA demonstrates favorable PHBHHx melt processability because the filaments and prints retain thermal stability even after three remelting cycles. Moreover, the addition of a high BTO content into the composite minimally affects its thermal stability and results in a slightly slower degradation process.

DSC thermograms contain several endothermic melting peaks during the first heating of all samples (figure 4(a)). Multiple peaks were also reported for different PHA-based materials and may be attributed to melt recrystallization and the formation of different crystalline regions [59]. Similar glass transition temperature $T_g \approx 4$ °C–5 °C in all samples (table 4) indicates that the amorphous phase of PHBHHx is mostly unaffected by remelting and high BTO content. The PHBHHx samples produce a broad melting peak at $T_m \approx 142$ °C (figure 4(b)), which is consistent with the earlier findings for Bluepha® PHBHHx [58]. F2 and P2 thermograms display higher intensity melting peaks (larger enthalpy ΔH_m), which results in slightly higher crystallinity of $X_c \approx 4.2\%$–4.8% in the double-extruded PHBHHx samples compared to the single-extruded F1 and P1 with $X_c \approx 1.1\%$–1.5%. An equivalent increase in biopolymer crystallinity is also observed in the double-extruded piezocomposites F2-BTO80, P2-BTO80 and P2-BTO80-P as compared to their single-extruded counterparts (table 4).

It is noted that the melting endotherm of P1 is particularly weak, which indicates a predominantly amorphous morphology in the single-extruded and printed neat PHBHHx. These observations are consistent with the TGA findings of the slightly reduced thermal stability of P1 (figure 3). It decomposes at a lower temperature with respect to the P2 sample (table 3), which is likely due to lower crystallinity, as the amorphous regions are thermally less stable than the crystalline ones. Furthermore, the lower crystallinity of P1 is also reflected in its slightly higher ductility because the fracture strain is marginally larger than that of P2 (section 3.2). Meanwhile, lower intensity but sharper melting peaks ($T_m \approx 132$ °C) are observed for the piezocomposites (figure 4(b)). Despite the lower total heat flow in the piezocomposites due to small 20% weight fraction of PHBHHx (reduced ΔH_m), the normalized crystallinity is slightly higher than of the neat biopolymer (table 4). Maximum values of $X_c \approx 10\%$–13% per gram of PHBHHx (equation (1)) were determined for the double-extruded piezocomposite. This suggests that BTO particles induce a mild nucleating effect that enhances the crystallization ability, as reported for PHB copolymers with inorganic modifiers [60], including ceramic-filled PHBHHx composites [61, 62]. Overall, we conclude that T_g and T_m of neat PHBHHx and BTO-rich piezocomposite remained relatively stable after repeated remelting during filament extrusion and 3D printing.

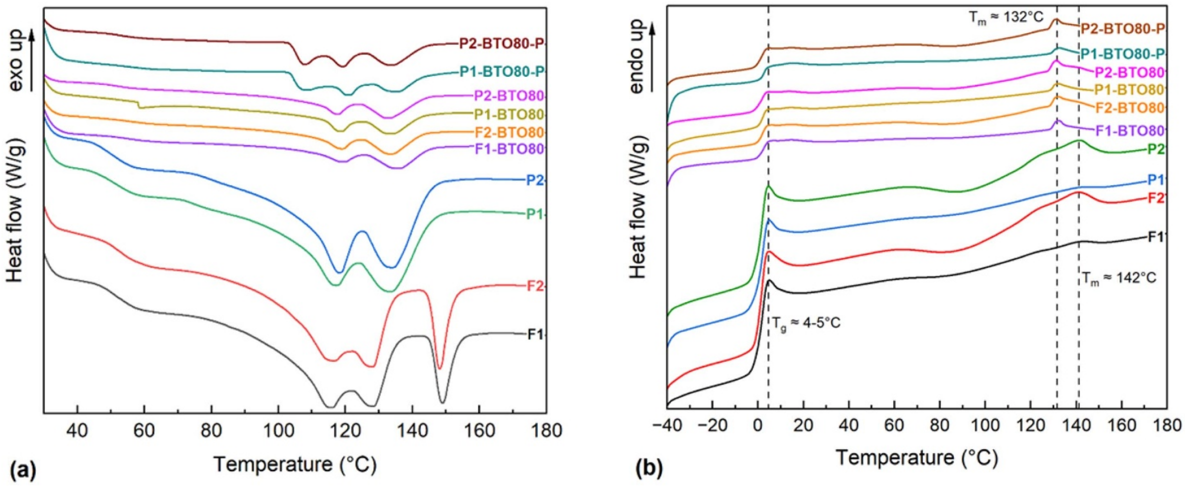

Figure 4. DSC thermograms for the single- and double-extruded PHBHHx and 20/80 wt% PHBHHx/BTO piezocomposite filaments and prints: (a) first and (b) second heating cycles.

Table 4. Thermal data derived from DSC measurements (second heating cycle): T_g—glass transition temperature, $T_{m(p)}$—melting temperature (peak), ΔH_m—enthalpy of melting, X_c—degree of crystallinity.

		Melting		
Sample	T_g (°C)	$T_{m(p)}$ (°C)	ΔH_m (J g^{-1})	X_c (%)
F1	4.7	142.5	1.667	1.45
F2	4.8	141.5	5.53	4.81
P1	4.9	142.2	1.272	1.05
P2	4.8	142.2	4.857	4.22
F1-BTO80	4.2	132.2	0.8252	3.59
F2-BTO80	4.5	131.9	2.657	11.56
P1-BTO80	4.7	132.1	1.242	5.40
P2-BTO80	4.5	131.6	2.449	10.65
P1-BTO80-P	4.5	132.5	0.567	2.47
P2-BTO80-P	4.2	132.1	2.909	12.65

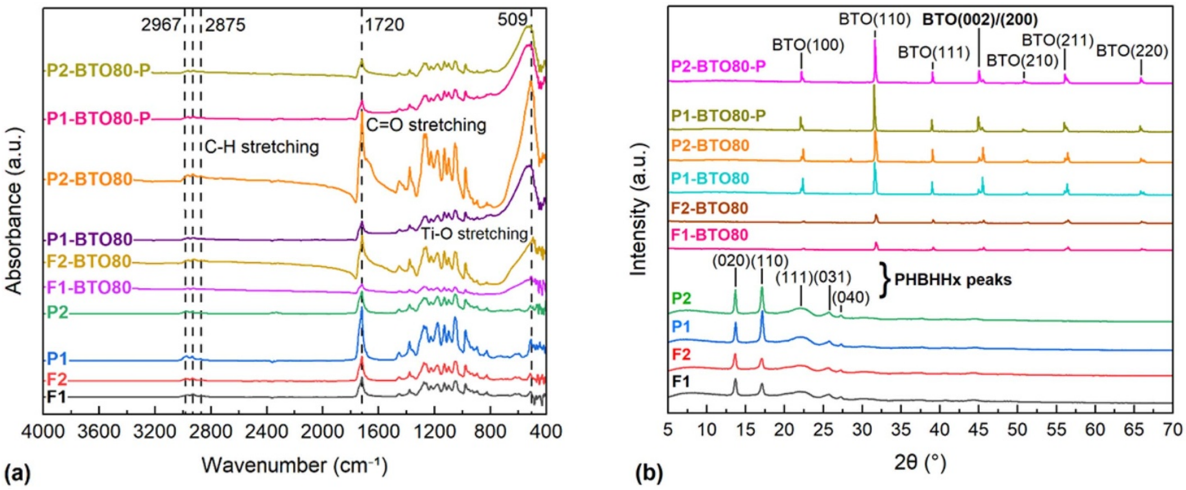

Figure 5. (a) FTIR spectra and (b) XRD patterns of single- and double-extruded PHBHHx and 20/80 wt% PHBHHx/BTO piezocomposite filaments and prints.

FTIR spectra in figure 5(a) reveal strong absorption band of PHBHHx at 1720 cm^{-1} that corresponds to the stretching vibration of the carbonyl groups (C=O) [63]. The peaks at 2967, 2935 and 2875 cm^{-1} are attributed to asymmetric and symmetric C–H stretching vibrations of methyl (–CH_3) and methylene (–CH_2–) groups. The bands

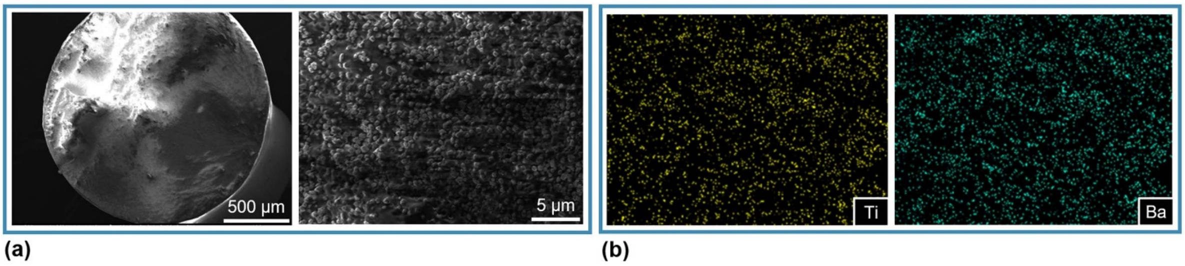

Figure 6. SEM-EDS analysis of the double-extruded 20/80 wt% PHBHHx/BTO filament (F2-BTO80): (a) SEM images of the cross-section, (b) distribution map of metal elements in BTO particles.

at 1450 and 1378 cm^{-1} are assigned to—CH_2—and—CH_3 bending vibrations, respectively. The broad region of 1400 and 1000 cm^{-1} corresponds to the—C–O—and—C–O–C—stretching vibrations [64]. The piezocomposite spectra display strong peaks in the 400–600 cm^{-1} range (Ti–O and Ti–O–T stretching modes in BTO [56]). They are more pronounced in the prints and slightly shift in the C=O stretching band. The absorption of the carbonyl (C=O) stretching vibration increases at 1720 cm^{-1} for the double-extruded F2-BTO80 and P2-BTO80 compared to the single-extruded samples. Overall, the FTIR results indicate that remelting did not noticeably affect the main spectral features and retained the chemical structure of PHBHHx [65].

PHBHHx diffraction peaks in figure 5(b) at 13.6°, 17.1°, 22.2°, 25.7° and 27.2° may be assigned to crystallographic planes characteristic of orthorhombic PHB-type crystalline structures: (020), (110), (111), (031) and (040), respectively [60]. The main peaks at 13.6° (020) and 17.1° (110) for prints P1 and P2 exhibit larger intensities, which suggests higher crystallinity compared to filaments F1 and F2. The peaks are not discernible in the XRD patterns of the piezocomposites, which are dominated by sharp diffraction signals from the abundant BTO particles. The peaks at 22.1°, 31.6°, 38.9°, 45°/45.5°, 50.8°, 56.3° and 65.8° correspond to the BTO lattice planes (100), (110), (111), (002)/(200), (210), (211) and (220) [66]. The presence of the ferroelectric tetragonal phase in BTO is identified in figure 5(b) by the characteristic peak splitting at $2\theta \approx 45^\circ$ (002)/(200) [66]. It confirms that BTO particles are electrically polarizable and the piezoresponse may be induced in the printed piezocomposite (section 3.3).

SEM micrographs reveal a uniform circular geometry of the double-extruded PHBHHx/BTO filament with densely packed and minimally agglomerated BTO particles (figure 6(a)). The effectiveness of the double-extrusion process is reflected in the SEM-EDS distribution of barium and titanium, which indicates a homogeneous filler dispersion (figure 6(b)). A homogeneous composition is advantageous for piezocomposite printability and polarizability, providing better consistency of the mechanical and piezoelectric properties of the prints.

3.2. Mechanical properties

The thermal impact during MEX should be controlled to achieve favorable mechanical properties of the 3D-printed PHBHHx-based components, including piezocomposite structures. Tensile tests were conducted at different strain rates to assess the effect of re-extrusion on the strength and ductility characteristics of the 3D-printed neat and BTO-rich PHBHHx thin-strip samples.

The stress-strain curves of PHBHHx samples P1 and P2 (figure 7(a)) reveal tensile responses that are typical for ductile polymers [55] and demonstrate strain-rate sensitivity common to deformed semi-crystalline polymers [67]. The samples exhibit broad plateaus of plastic deformation at larger stress levels, which indicates higher toughness and resistance to abrupt failure. No significant differences are observed in the strength and ductility of P1 and P2 (figures 7(b) and (c)). Except, at the lowest speed of 10 mm min^{-1}, the P2 samples display slightly lower fracture strain levels, while they are comparable at higher strain rates. Overall, the results indicate that PHBHHx remelting during filament re-extrusion and printing had no detrimental impact on the mechanical properties.

The strain-rate-dependent strengthening effect manifests in the PHBHHx samples when the loading speed increases by two orders of magnitude (strain rate range of 0.0017–0.17 s^{-1}). The tensile strength of P1 and P2 is increased by 32% from an average value of ~22 MPa at 10 mm min^{-1} to the ~29 MPa at 1000 mm min^{-1} (figure 7(b)). The yield strain does not exhibit strain-rate sensitivity and shows comparable average values of ~9%–10% for P1 and P2 (figure 7(c)). In contrast, the fracture strain (elongation at break) demonstrates a larger dispersion of values, which is expected, as it is typically more sensitive to microstructural fluctuations in thermally processed semi-crystalline polymers [68]. In the 3D-printed PHBHHx samples, such fluctuations in structural quality may be attributed to variability in the extent of micro-voids, which are likely to occur at imperfectly fused interfaces. A moderate degree of strain-rate-dependent hardening behavior is evidenced by a slight reduction in average fracture strains of P1 and P2 samples at higher speeds of 100–1000 mm min^{-1} (~15%–17%) compared to 10 mm min^{-1} (~18%–21%). Such a reduction in ductility with faster material deformation is consistent with the strain-rate-dependent tensile responses of other thermoplastic polymers [67].

Contrary to the ductile behavior of PHBHHx, the piezocomposite responds to loading in a brittle-like manner (figure 7(a)). It undergoes sudden rupture without noticeable

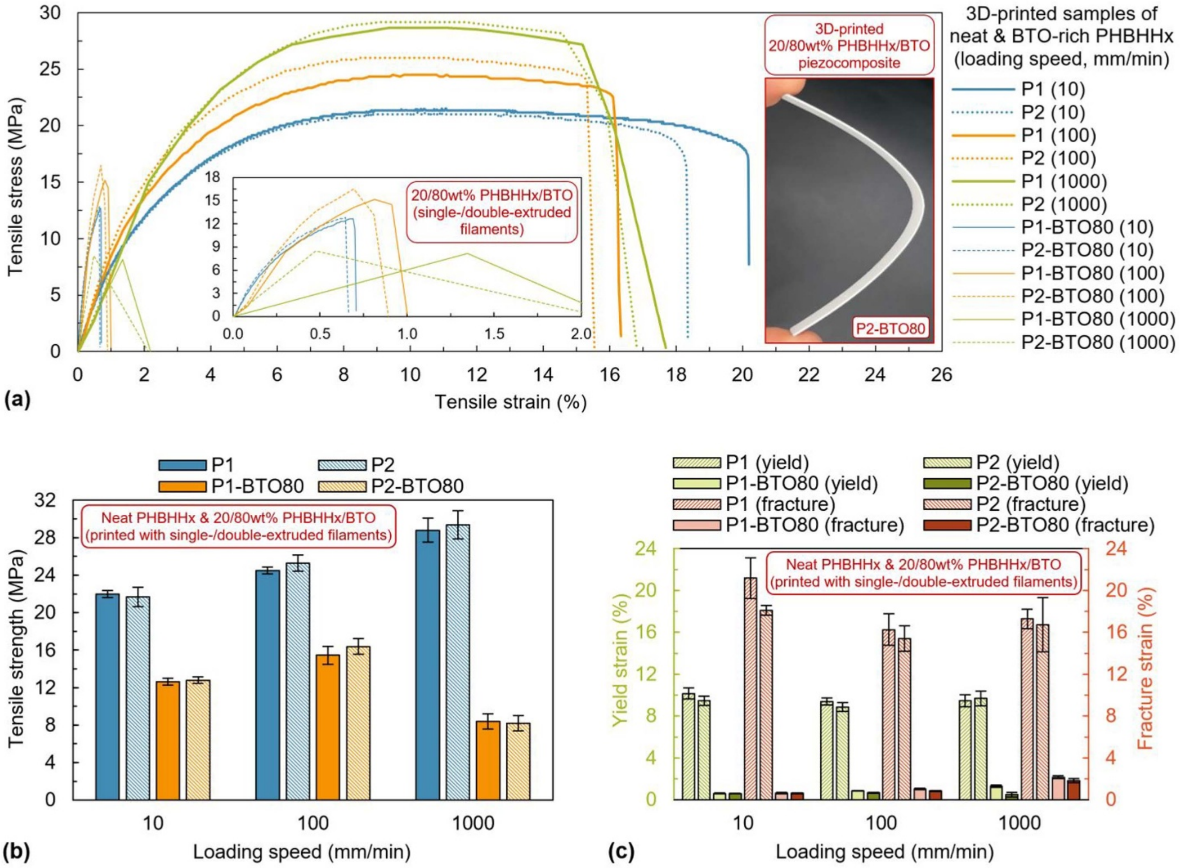

Figure 7. (a) Tensile responses and (b-c) mechanical properties of 3D-printed thin strips of single- and double-extruded neat PHBHHx and 20/80 wt% PHBHHx/BTO piezocomposite tested at different loading speeds (range of 10–1000 mm min^{-1}).

plastic yielding and reaches significantly lower fracture strains (∼0.6%–2.2% depending on strain rate (figure 7(c))). The piezocomposite exhibits inferior mechanical properties compared to PHBHHx prints. A similar decrease in the properties was also reported for the PHB composite with a low BTO content of 5–20 wt% [31]. In our case, much higher BTO content leads to ∼41% reduction in average tensile strength (∼13 MPa vs. ∼22 MPa for PHBHHx at 10 mm min^{-1}). It could be presumed that high filler content may easily result in pronounced particle agglomerations, as it is a common phenomenon, including the PHA-based composites [69]. Some agglomerations are unavoidable, and they would act as multiple stress concentrators, weakening the composite due to the extensive crack initiation sites [70]. However, agglomerations appear to be minimal (figures 6(a)), and a more plausible underlying cause for the reduced strength is poor adhesion at the interface between the PHBHHx matrix and BTO particles. This may be attributed to the polarity mismatch because the as-received (unmodified) BTO likely possesses intrinsically polar and hydrophilic surface hydroxyl groups [71]. This reduces filler-matrix adhesion due to the weaker chemical affinity with the less polar and relatively hydrophobic PHBHHx [9]. This claim is supported by the finding that piezocomposite re-extrusion, acting as an agglomeration-reducing process, has a negligible effect on the strength (figure 7(b)). Moreover, if extensive BTO agglomerations were the primary cause, re-extrusion would likely have a positive reinforcing effect (as observed in our previous study using the same BTO filler dispersed in a highly polar fluoropolymer PVDF-HFP [56]).

The piezocomposite stiffness increased by nearly 3.5 times with respect to that of neat PHBHHx (average tensile modulus of ∼3180 MPa vs. ∼920 MPa (figure S1)). However, even at ∼45 vol% BTO, the piezocomposite retains acceptable flexibility (figure 7(a)). Although moderate, it would be sufficient for many load-bearing components operating under small to medium deflections (e.g. sensor-integrated structures subjected to bending in unmanned aircrafts that often rely on less sustainable lead-based piezoceramics for structural health monitoring [72]).

Interestingly, mild strain-rate-dependent softening is observed, as the fracture strain of the piezocomposite slightly improves at higher loading speed (figure 7(c)). This is in contrast to the more common hardening and embrittlement effects reported for many polymer composites at higher strain rates [70]. This unusual behavior suggests that in the BTO-rich piezocomposite, the conventional failure mechanism (initiated by filler-matrix debonding [70]) becomes more complex, possibly because of the dominant influence of the abundant hard particles. In addition, figure 7(b) reveals a more intricate and less favorable strain-rate dependency of the tensile

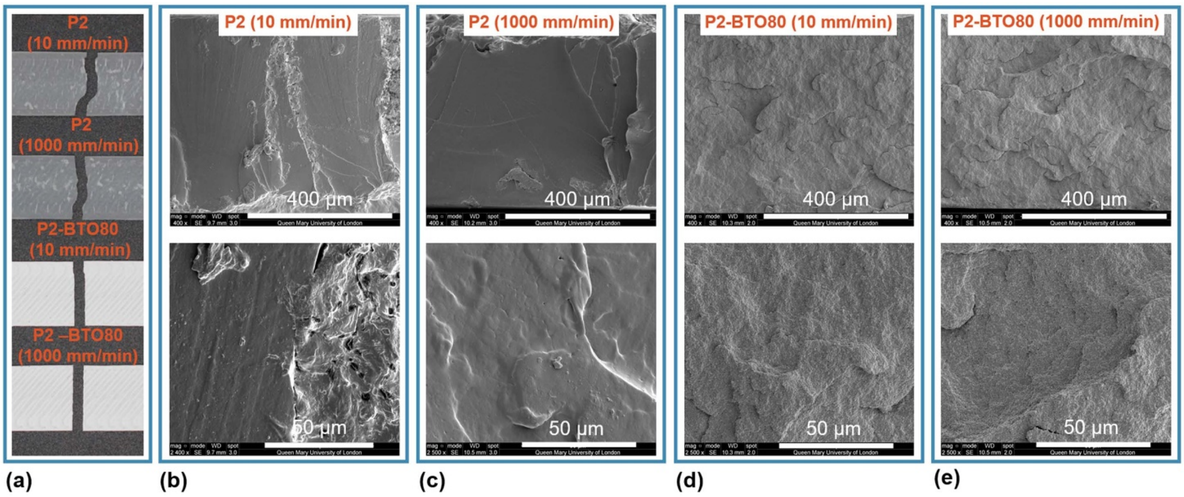

Figure 8. (a) Optical images and (b)–(e) SEM fractographs of 3D-printed thin-strip samples of PHBHHx (P2) and 20/80 wt% PHBHHx/BTO piezocomposite (P2-BTO80), ruptured at 10 and 1000 mm min^{-1}.

strength. Initially, it increases by 23% from $\sim$13 to $\sim$16 MPa at 10 and 100 mm min^{-1}, respectively. This indicates typical strain-rate strengthening, which is consistent with the behavior of neat PHBHHx. However, at the highest loading speed of 1000 mm min^{-1}, the tensile strength is reduced by 50% to $\sim$8 MPa, suggesting a premature failure. This may be attributed to poor filler-matrix interfacial adhesion and the unavoidable presence of some BTO agglomerations, which act as stress concentrators and initiate interfacial defects. It is reasonable to assume that under more rapid deformation at 1000 mm min^{-1}, stresses around the defects can no longer be effectively dissipated because the stress relaxation time is known to diminish at higher strain rates [70]. This promotes micro-crack formation and propagation, ultimately leading to premature failure. It is likely that poor BTO-PHBHHx interfacial adhesion is the dominant cause of this strength reduction at 1000 mm min^{-1}, as suggested by the SEM fractographs (figure 8). Moreover, such a weakening effect at higher strain rates was not observed in a comparable BTO-rich PVDF-based piezocomposite, which is characterized by a stronger filler-matrix bonding due to more polar matrix [56].

The macroscopic fracture patterns of neat PHBHHx prints (figure 8(a)) demonstrate a strain-rate-dependent transition from a moderately ductile to a brittle-like failure mode. At 10 mm min^{-1}, the fracture path of P2 sample is uneven (zigzag-like) without visible necking, which suggests a moderately ductile rupture. At 1000 mm min^{-1}, the fracture path is straighter and more uniform, indicating reduced ductility and a shift toward brittle-like rupture. The SEM fractographs further support these observations because at 10 mm min^{-1}, we note typical features of moderately ductile fracture. They include a rough surface morphology with some shear bands, micro-voids and fibrillated microstructures, which are associated with plastic flow and energy dissipation (figure 8(b)). A similar fracture surface morphology was also observed in another study on PHBHHx [73]. In contrast, the rupture at 1000 mm min^{-1} produces a smoother and cleaner surface morphology with straight fracture edges and cleavage-like features (figure 8(c)), which indicate minimal plastic deformation and a brittle-like failure mode. This surface morphology obtained at the highest strain rate is comparable to the fracture patterns obtained at lower strain rates in less ductile scl-PHAs [74].

The BTO-rich piezocomposite (P2-BT80) ruptures predominantly as a brittle material both at low and high strain rates, which is visible from the relatively straight and micro-jagged macroscopic fracture path compared to neat PHBHHx prints (figure 8(a)). The brittle failure mode is also evident in the SEM fractographs that show no signs of fibrillar features (figures 8(d) and (e)). Instead, they display a uniformly rough, irregular and stepped surface morphology with angular facets and cleavage-like steps (layered lamellar-type microstructures are visible at lower SEM magnification). A similar rough surface morphology was also reported in another study on PHBHHx/BTO piezocomposite [33].

Overall, we emphasize that due to brittle fracture behavior, reduced tensile strength and ductility, additional care should be exercised when designing ceramic-rich piezocomposite sensors to ensure their operation within the allowable deformation range to prevent premature failure.

3.3. *Piezoelectric performance*

An expected tendency of d_{33} amplification with increasing external poling field E_{ext} and duration t_{ext} [75] is evident in figure 9 (it presents stable d_{33} values after the initial post-poling decay). A compensating relationship is observed between the t_{ext} and E_{ext}, as the reduction in one parameter (e.g. shorter poling) may be balanced in some cases by increasing the other (e.g. stronger field) to produce comparable d_{33} levels. For example, ultra-short poling for 2 s at 18.2 kV mm^{-1} produces similar d_{33} of $\sim$3.2–3.6 pC/N as the 1000 s poling at 5-fold lower field of 3.64 kV mm^{-1}. Comparison of d_{33} at 2 s and 1000 s (figure 9(a)) reveals that d_{33} dependence on t_{ext} is very strong at smaller E_{ext} ($\lesssim$7 kV mm^{-1}), while it is weaker and becomes comparable at larger E_{ext} ($\gtrsim$14 kV mm^{-1}).

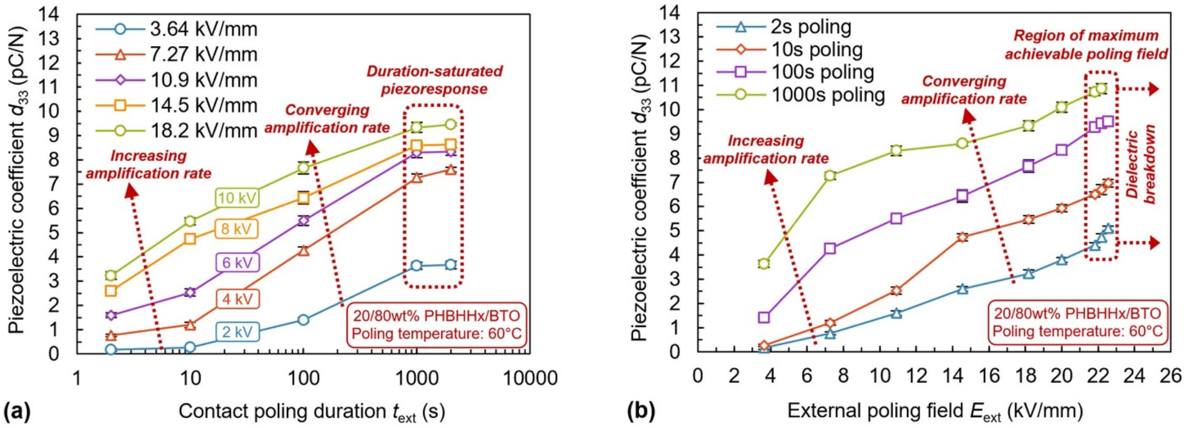

Figure 9. Longitudinal piezoresponse of 20/80 wt% PHBHHx/BTO piezocomposite as a function of: (a) contact poling duration t_{ext} at increasing external field E_{ext} (poling voltage of 2–10 kV), (b) E_{ext} increased until the maximum achievable pre-breakdown magnitude during poling within the range $t_{ext} = 2$–1000 s.

Piezoresponse dependences on t_{ext} or E_{ext} contain several distinct regions with different rates of change (slopes $\Delta d_{33}/\Delta t_{ext}$ and $\Delta d_{33}/\Delta E_{ext}$ in figure 9). The region of increasing d_{33} amplification rate $\Delta d_{33}/\Delta t_{ext}$ is characteristic to the short-duration poling regime at $t_{ext} \approx 2$–10 s (figure 9(a)). A more pronounced field dependence is observed here because stronger fields ($E_{ext} \approx 14$–18 kV mm^{-1}) produce a markedly larger increase in d_{33} than weaker fields ($E_{ext} \approx 4$–11 kV mm^{-1}). In the medium-duration poling regime (t_{ext} of 10 s to 100s seconds), the d_{33} amplification rates at weaker and stronger fields become comparable. In the long-duration poling regime ($t_{ext} > 1000$ s), d_{33} becomes largely insensitive to further increase in t_{ext}, which manifests as d_{33} plateau (values cluster around ~7–9 pC/N at larger E_{ext}). It indicates that a duration-saturated polarization level was reached in the BTO particles for $t_{ext} \approx 1000$–2000 s at all fields. In contrast, no plateau is identified in the field-dependent d_{33} plots, though they also contain regions of increasing ($\lesssim$7 kV mm^{-1}) and converging ($\gtrsim$7 kV mm^{-1}) d_{33} amplification rate (figure 9(b)). The absence of the field-dependent d_{33} plateau suggests that the duration-saturated d_{33} values at $t_{ext} \approx 1000$–2000 s (figure 9(a)) correspond to the field-limited polarization in the BTO particles. Thus, even the strongest achieved field of ~22.2–22.5 kV mm (figure 9(b)) is insufficient to induce both the field- and duration-saturated (i.e. complete) polarization state in BTO for producing higher d_{33} levels.

The piezocomposite essentially has 0–3 connectivity due to randomly dispersed BTO particles that are mostly isolated and interspaced by the interconnected PHBHHx matrix (figure 6). However, achieving a complete polarization saturation state in a ferroelectric filler is very challenging for 0–3 piezocomposites. Therefore, the poling efficiency and resulting d_{33} levels are inherently very limited compared to bulk piezoceramics [20]. For example, at $E_{ext} = 3.64$ kV mm^{-1} and $t_{ext} = 1000$ s, the d_{33} is very small (~3.6 pC/N), while in bulk BTO it can reach ~150 pC/N under polarization saturation state achieved using nearly identical poling parameters [76]. This inferior performance is attributed to the orders-of-magnitude mismatch in the permittivity and resistivity of BTO and PHBHHx. The expected values are: $\varepsilon_f \approx 1200$–1500 [66], $\varepsilon_m \approx 5$ [77], $\rho_f \approx 10^9$ Ω·cm [56], $\rho_m \approx 10^{11}$–10^{13} Ω·cm [77, 78]. When external field E_{ext} is applied, the effective electrical field (E_{eff}) that acts on high-permittivity BTO particles is considerably smaller because it is partially screened by the low-permittivity PHBHHx matrix (i.e. $\varepsilon_m/\varepsilon_f \ll 1$) [79]. Therefore, a relatively strong field of $E_{ext} \gtrsim 18$–20 kV mm^{-1} is needed to achieve higher d_{33} levels (figure 9(b)), even though the coercive field of BTO is much smaller ($E_c \lesssim 1$ kV mm^{-1} [76]). Overall, E_{ext} levels approximately an order of magnitude higher than E_c are required (~7–11 kV mm^{-1}) to produce more appreciable piezoresponses after minutes-range poling. For $t_{ext} > 1000$ s, the highest d_{33} of ~7–11 pC/N is achieved by applying fields of $\gtrsim$7 kV mm^{-1}. Meanwhile, stronger fields of $\gtrsim$11–14 kV mm^{-1} are needed to induce more adequate d_{33} levels after seconds-range poling. Interestingly, even ultra-short poling for 2–10 s can produce useable ~5–7 pC/N levels when applying the strongest field of $E_{ext} \approx 22.5$ kV mm^{-1}. The strongest achievable field tends to decrease slightly for longer durations of $\geqslant$1000 s because the likelihood of breakdown increases with time (22.2 kV mm^{-1} was the maximum field achieved at 1000 s).

In principle, for a given filler content, the poling efficiency of a piezocomposite is governed by the ratio E_{eff}/E_{ext}, which is increased by minimizing the permittivity and resistivity mismatches between the filler and the matrix. Essentially, E_{eff} nonlinearly depends on the ratios $\varepsilon_m/\varepsilon_f$ and ρ_f/ρ_m according to the simplified Maxwell–Wagner model [79]. Because $\varepsilon_m/\varepsilon_f \ll 1$, the effective dielectric constant ε_{eff} of the piezocomposite is dominated by ε_m [80]. This implies that the permittivity of the polymer matrix largely determines the poling efficiency and the maximum achievable d_{33} levels. Therefore, it is advantageous that the permittivity of PHBHHx ($\varepsilon_m \approx 5$ [77]) is higher than that of many common polymers (typically $\varepsilon_m \approx 2$–4 [79, 80]), except for PVDF-based polymers (typically $\varepsilon_m > 8$–9). Furthermore, a moderate reduction

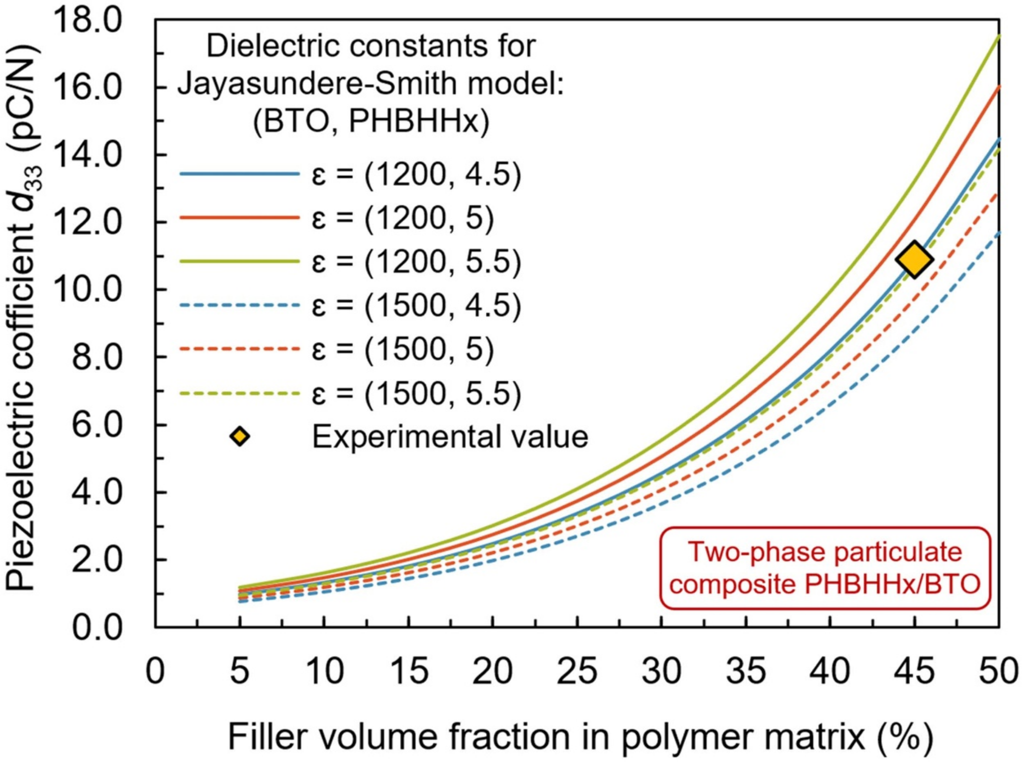

Figure 10. Comparison of the measured maximum d_{33} with the predictions of the Jayasundere–Smith piezoresponse model for two-phase particulate composites [80] (dielectric constants are based on [66, 77]).

in matrix resistivity during poling (bringing ρ_m closer to ρ_f but avoiding breakdown) may reduce the E_{ext} level needed to maximize d_{33} [80]. It is plausible that poling efficiency also benefits from lower PHBHHx resistivity ($\rho_m \approx 10^{11}$–10^{13} Ω·cm [77, 78]) compared to many polymers (commonly $\rho_m > 10^{14}$ Ω·cm [79]). Additionally, the applied poling at 60 °C further enhances poling efficiency, as previous study on PHB copolymer suggests that ρ_m could be reduced by up to an order of magnitude compared with the room-temperature case [81]. Thus, it is likely that ρ_m of the PHBHHx matrix is also reduced at 60 °C, which may bring ρ_m closer to ρ_f and amplify the effective poling field, as E_{eff}/E_{ext} depends on ρ_f/ρ_m [79]. Furthermore, the positive effect of thermal poling is also attributed to the enhanced dipole alignment in the BTO particles (better ferroelectric polarizability). It is known that lattice ions and domain walls become more mobile above the room temperature (below the Curie point of ∼120 °C), which reduces E_c of BTO and improves poling efficiency [56].

The highest d_{33} of 10.9 ± 0.21 pC/N (figure 9(b)) was measured after poling at a maximum achieved field of 22.2 kV m^{-1} for a saturation poling duration of 1000 s (this matches the duration needed for polarization saturation of bulk BTO [76]). The achieved maximum piezoresponse of ∼11 pC/N is noteworthy when compared to similar two-phase 0–3 piezocomposites that are formed as solid sheets (non-fibrous), consisting of a low-permittivity polymer matrix filled with conventional piezoceramics (i.e. the BTO grade used herein). The value of ∼11 pC/N exceeds several times the d_{33} of other PHA/BTO piezocomposites (∼0.7–1.5 pC/N [32, 33, 35]), though their fill factors were lower (⩽25 vol%). It is more pertinent to compare against the poled piezocomposites with high piezoceramic content of ∼40–50 vol%. The measured maximum piezoresponse is also higher than the ∼6 pC/N reported for the PHB composite with 50 vol% PZT [30]. It is also slightly higher than ≲10 pC/N levels reported for the BTO-rich piezocomposites based on conventional polymers [80]. For comparison, the reported piezoresponses for neat PHAs are typically ≲5 pC/N (in fibrous samples [24–28]), and ≲1 pC/N for the molded sample of neat PHBHHx [23]. We note that the measured value of ∼11 pC/N agrees well with the prediction of the Jayasundere–Smith model (figure 10), which is applicable for the higher-filled particulate composites and is relatively accurate in the 40–50 vol% filler range [80].

The analysis of piezoresponse stabilization shortly after poling demonstrates that the combined effect of the poling field and duration has a strong impact on the level of initial depolarization in the piezocomposite (figure 11). This partial short-term loss of polarization reflects the capability of retention of the induced dipole alignment in BTO and is a typical behavior of 0–3 piezocomposites. Depolarization leads to transient piezoresponse decay over the next two days after poling (post-poling time $t_{pp} \approx 0.03$–56 h). It is evaluated as the relative d_{33} decrease Δ_{pp} (figure 11(b)), which is calculated using values measured immediately after poling ($t_{pp} \approx 2$ min) and after two days ($t_{pp} \approx 56$ h).

For all E_{ext} and t_{ext} values used in this study, the d_{33} magnitudes were found to stabilize after one day (figure 11(a)), which is illustrated by the d_{33} plateau at $t_{pp} = 28$–56 h (for

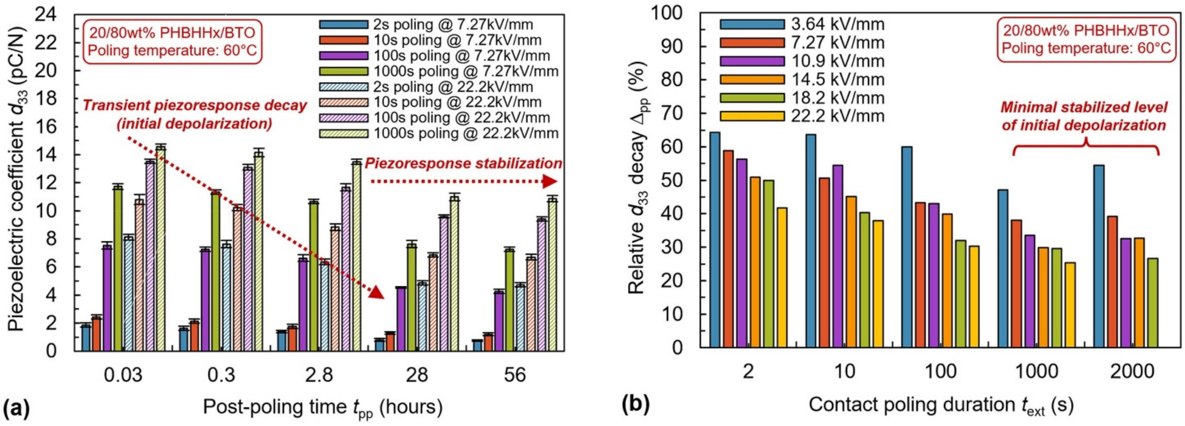

Figure 11. (a) Post-poling transient d_{33} decay of the 20/80 wt% PHBHHx/BTO piezocomposite after short- and long-duration contact poling at relatively weak and strong fields E_{ext}. (b) Relative d_{33} decrease Δ_{pp} (d_{33} values measured immediately and ~2 d after poling) as a function of poling duration t_{ext} at different fields E_{ext}.

a specific t_{ext}). Longer poling with stronger fields is advantageous for piezoelectric stability, as shown by the decrease in relative d_{33} decay levels with larger E_{ext} and t_{ext} (figure 11(b)). The decay becomes minimal and stabilizes after long-duration poling for $\geqslant$1000 s, except for the 3.64 kV mm^{-1} case, where Δ_{pp} remains high and tends to fluctuate. Meanwhile, at strong poling fields of $\gtrsim$18 kV mm^{-1}, the Δ_{pp} levels exhibit more substantial drop after the short 100 s poling compared to the 2–10 s case (~30% vs. ~40%–50%). The minimum depolarization is observed after the long-duration poling at the strongest field (1000 s, 22.2 kV mm^{-1}), where d_{33} decays from the initial ~15 pC/N to a stable value of ~11 pC/N ($\Delta_{pp} \approx 25\%$). In contrast, poling at the 6-fold weaker field of 3.64 kV mm^{-1} results in maximum depolarization ($\Delta_{pp} \approx 47\%$–64%), which remains pronounced even at $t_{ext} \geqslant 1000$ s. Interestingly, ultra-short poling for 2–10 s at 22.2 kV mm^{-1} produces d_{33} decay levels similar to the measured after the 1000 s poling at 3-fold weaker field of 7.27 kV mm^{-1} ($\Delta_{pp} \approx 40\%$). Overall, it is noted that seconds-range poling at 60 °C with the strongest field of ~22 kV mm^{-1} can induce useable piezoresponses (~5–7 pC/N), which exhibit adequate charge stability compared to the minutes-range poling regime (Δ_{pp} of ~40% vs. ~25%).

The achieved d_{33} levels are sufficient to justify further integration of the piezocomposite into fully FFF-printed functional piezo-devices (e.g. vibration sensors). To enable monolithic integration (co-printing) of electrodes during FFF of the piezocomposite, we are completing the development of a PHBHHx conductive composite filament doped with graphene nanoplatelets. The resistivity of the filament is relatively high (~0.5–1 Ω·cm), but it is comparable to the best available commercial filaments with carbonaceous fillers [82]. Our initial experiments indicate that it is feasible to print moderately conductive electrodes and apply them for effective poling and piezoelectric signal collection (though piezo-charge dissipation in the resistive electrodes reduces the maximum achievable d_{33}). Moreover, other group has previously demonstrated the feasibility of this approach [83] using non-biodegradable piezocomposite and a poorly conductive commercial filament (NinjaTek EEL™ [82]).

4. Conclusions

3D printing filaments of neat and BTO-rich PHBHHx were produced, printed and tested to demonstrate the economical, scalable and more sustainable (solvent-free) extrusion-based manufacturing of eco-friendly piezocomposites. Physicochemical and tensile tests indicate that PHBHHx can be successfully used for composite manufacturing via melt reprocessing. The re-extruded PHBHHx retains chemical structure, thermal stability, predominantly amorphous morphology and favorable mechanical properties after three remelting cycles (single or double extrusion near the melting point of 130 °C–140 °C and FFF at 170 °C). The re-extrusion workflow ensures the uniform dispersion of BTO particles, which exert a mild nucleating effect and slightly increase low crystallinity of PHBHHx. The FFF process was fine-tuned to print well-fused piezocomposites that display adequate mechanical properties and relatively strong piezoresponses of up to ~11 pC/N owing to excellent high-field poling stability (up to ~22 kV mm^{-1} at 60 °C). Moreover, high-field ultra-short poling for several seconds produces useable d_{33} levels of ~5–7 pC/N. The ductile PHBHHx matrix provides moderate piezocomposite flexibility, which can be sufficient for many piezoelectric sensors operating in load-bearing components under small-to-medium deflections. Neat PHBHHx exhibits strain-rate-dependent strengthening and hardening effects, whereas the piezocomposite exhibits strengthening, weakening and mild softening depending on the strain rate. Because of high BTO content (~45 vol%) and weaker filler-matrix interfacial adhesion, the tensile strength and ductility were reduced compared to neat PHBHHx. This indicates that the design of piezocomposite sensors requires careful consideration of actual dynamic loading conditions to prevent premature failure. It is important for future research to explore compositional modifications that enhance filler-matrix bonding and composite toughness, while preserving its eco-safety profile (e.g. by introducing more polar biodegradable copolymer). Overall, the implemented melt-based workflow relies on affordable desktop machines, which supports the ongoing democratization of MEX AM technologies. The workflow is scalable to larger volume manufacturing of PHBHHx composite filaments or pellets filled with densely packed hard particles.

Data availability statement

The data that support the findings of this study are available upon reasonable request from the authors.

Supplementary table and plots available at https://doi.org/10.1088/1748-9326/ae1e14/data1.

Acknowledgments

This research work has received funding from the Research Council of Lithuania (LMTLT) under the Agreement No. S-MIP-25-47 for the project 'Co-extrusion additive manufacturing of eco-friendly natural fiber-reinforced sensorized composites for safety-critical lightweight structures (AM-ECO-SENSE)'.

Conflict of interest

The authors declare that there is no conflict of interest.

Ethical approval

This study does not contain any studies with human or animal subjects performed by any of the authors.

Author contributions

Malik Daniyal Zaheer 0000-0001-7570-8773
Conceptualization (equal), Data curation (lead), Formal analysis (equal), Investigation (lead), Methodology (equal), Validation (equal), Visualization (equal), Writing – original draft (lead)

Rolanas Dauksevicius 0000-0002-4571-757X
Conceptualization (equal), Formal analysis (equal), Funding acquisition (lead), Methodology (equal), Resources (equal), Supervision (lead), Validation (equal), Visualization (equal), Writing – review & editing (lead)

Qasim Zia 0000-0001-7823-3136
Data curation (supporting), Investigation (equal), Methodology (equal), Resources (equal), Validation (supporting), Visualization (supporting)

Madeeha Tabassum 0000-0001-7911-4913
Data curation (supporting), Investigation (supporting), Methodology (supporting), Resources (supporting), Visualization (supporting)

References

[1] Min J, Jung Y, Ahn J, Lee J G, Lee J and Ko S H 2023 Recent advances in biodegradable green electronic materials and sensor applications *Adv. Mater.* **35** 2211273

[2] Tan H W, Choong Y Y C, Kuo C N, Low H Y and Chua C K 2022 3D printed electronics: processes, materials and future trends *Prog. Mater. Sci.* **127** 100945

[3] Yuan X, Mai Z, Li Z, Yu Z, Ci P and Dong S 2023 A 3D-printing approach toward flexible piezoelectronics with function diversity *Mater. Today* **69** 160–92

[4] Wolstrup A F, Spangenberg J, Yamamoto A, Gleadall A and Zsurzsan G 2025 Advances in 3D printed electromechanical sensors: performance comparison, trends, and future directions *Addit. Manuf.* **106** 104799

[5] Persano L *et al* 2024 Advanced materials for energy harvesting and soft robotics: emerging frontiers to enhance piezoelectric performance and functionality *Adv. Mater.* **36** 2405363

[6] Li S, Shan Y, Chen J, Chen X, Shi Z, Zhao L, He R and Li Y 2025 3D printing and biomedical applications of piezoelectric composites: a critical review *Adv. Mater. Technol.* **10** 2401160

[7] Guggenbiller G, Brooks S, King O, Constant E, Merckle D and Weems A C 2023 3D printing of green and renewable polymeric materials: toward greener additive manufacturing *ACS Appl. Polym. Mater.* **5** 3201–29

[8] Yousefi A M and Wnek G E 2025 Poly(hydroxyalkanoates): emerging biopolymers in biomedical fields and packaging industries for a circular economy *Biomed. Mater. Devices* **3** 19–44

[9] Eraslan K, Aversa C, Nofar M, Barletta M, Gisario A, Salehiyan R and Goksu Y A 2022 Poly(3-hydroxybutyrate-co-3-hydroxyhexanoate) (PHBH): synthesis, properties, and applications—a review *Eur. Polym. J.* **167** 111044

[10] Owusu F, Venkatesan T R, Nüesch F A, Negri R M and Opris D M 2023 How to make elastomers piezoelectric? *Adv. Mater. Technol.* **8** 2300099

[11] Valentini F, Dorigato A, Rigotti D and Pegoretti A 2019 Polyhydroxyalkanoates/fibrillated nanocellulose composites for additive manufacturing *J. Polym. Environ.* **27** 1333–41

[12] Kovalcik A, Sangroniz L, Kalina M, Skopalova K, Humpolíček P, Omastova M, Mundigler N and Müller A J 2020 Properties of scaffolds prepared by fused deposition modeling of poly(hydroxyalkanoates) *Int. J. Biol. Macromol.* **161** 364–76

[13] Cappiello G, Aversa C, Barletta M and Gisario A 2023 Progress in design and processing of polyhydroxyalkanoates (PHAs): home compostable poly(3-hydroxybutyrate-co—3-hydroxyhexanoate) (PHBHHx)/polybutylene succinate-co-adipate (PBSA) blend *J. Appl. Polym. Sci.* **140** e53933

[14] Vanheusden C, Samyn P, Vackier T, Steenackers H, D'Haen J, Peeters R and Buntinx M 2024 Fabrication of Poly(3-hydroxybutyrate-co-3-hydroxyhexanoate)/ZnO nanocomposite films for active packaging applications: impact of ZnO type on structure–property dynamics *Polymers* **16** 1861

[15] Ivorra-Martinez J, Peydro M Á, Gomez-Caturla J, Sanchez-Nacher L, Boronat T and Balart R 2023 The effects of processing parameters on mechanical properties of 3D-printed polyhydroxyalkanoates parts *Virtual Phys. Prototyp.* **18** e2164734

[16] Ivorra-Martinez J, Gomez-Caturla J, Peydro M A, Selles M A and Boronat T 2024 Commercial grade of P(3HB- co -3HHX) final properties adjustment by the modification of cooling conditions in the injection molding and ageing process *Macromol. Mater. Eng.* **309** 2400033

[17] Ďurfina M, Babaei N, Vanovčanová Z, Feranc J, Horváth V, Vašková I, Kruželák J, Tomanová K and Plavec R 2025 Bio-based polyhydroxyalkanoate (PHA) blends for 3D printing: rheological, mechanical, biocompatibility, and biodegradation properties *Polymers* **17** 1477

[18] Hiller T, Gutbrod F, Bonten L, Vocht M P, Azimian M, Resch J, Bonten C and Winnacker M 2024 Generation of bio-based, shape- and temperature-stable three-dimensional nonwoven structures using different polyhydroxyalkanoates *Polymers* **17** 51

[19] Eesaee M, Ghassemi P, Nguyen D D, Thomas S, Elkoun S and Nguyen-Tri P 2022 Morphology and crystallization behaviour of polyhydroxyalkanoates-based blends and composites: a review *Biochem. Eng. J.* **187** 108588

[20] Eltouby P, Shyha I, Li C and Khaliq J 2021 Factors affecting the piezoelectric performance of ceramic-polymer composites: a comprehensive review *Ceram. Int.* **47** 17813–25

[21] Khan A, Joshi R, Sharma M K, Huang C-J, Yu J-H, Wang Y-L and Lin Z-H 2024 The potential of organic piezoelectric materials for next-generation implantable biomedical devices *Nano Trends* **6** 100032

[22] Fukada E and Ando Y 1986 Piezoelectric properties of poly-β-hydroxybutyrate and copolymers of β-hydroxybutyrate and β-hydroxyvalerate *Int. J. Biol. Macromol.* **8** 361–6

[23] Takarada J, Yoshida K, Tanaka Y, Magori Y, Kawakami K, Mukai M, Yamashita Y, Tsuneishi H and Tajitsu Y 2024 Microscopic and macroscopic evaluations of piezoelectric properties of PHBH fiber and film *Jpn. J. Appl. Phys.* **63** 09SP26

[24] Cai Z, Xiong P, He S and Zhu C 2019 Improved piezoelectric performances of highly orientated poly(β-hydroxybutyrate) electrospun nanofiber membrane scaffold blended with multiwalled carbon nanotubes *Mater. Lett.* **240** 213–6

[25] Zviagin A S, Chernozem R V, Surmeneva M A, Pyeon M, Frank M, Ludwig T, Tutacz P, Ivanov Y F, Mathur S and Surmenev R A 2019 Enhanced piezoelectric response of hybrid biodegradable 3D poly(3-hydroxybutyrate) scaffolds coated with hydrothermally deposited ZnO for biomedical applications *Eur. Polym. J.* **117** 272–9

[26] Konuk Tokak E, Çetin Altındal D, Akdere Ö E and Gümüşderelioğlu M 2021 In-vitro effectiveness of poly-β-alanine reinforced poly(3-hydroxybutyrate) fibrous scaffolds for skeletal muscle regeneration *Mater. Sci. Eng. C* **131** 112528

[27] Chernozem R V, Guselnikova O, Surmeneva M A, Postnikov P S, Abalymov A A, Parakhonskiy B V, De Roo N, Depla D, Skirtach A G and Surmenev R A 2020 Diazonium chemistry surface treatment of piezoelectric polyhydroxybutyrate scaffolds for enhanced osteoblastic cell growth *Appl. Mater. Today* **20** 100758

[28] Chernozem R V *et al* 2019 Piezoelectric 3-D fibrous Poly(3-hydroxybutyrate)-based scaffolds ultrasound-mineralized with calcium carbonate for bone tissue engineering: inorganic phase formation, osteoblast cell adhesion, and proliferation *ACS Appl. Mater. Interfaces* **11** 19522–33

[29] Sugita A, Mitsubayashi M and Tasaka S 2006 Electric activity in rigid rod-like polymer, poly(β-hydroxybutyrate) *Polymer* **47** 5141–4

[30] Malmonge J A, Malmonge L F, Fuzari G C, Malmonge S M and Sakamoto W K 2009 Piezo and dielectric properties of PHB–PZT composite *Polym. Compos.* **30** 1333–7

[31] Strangis G *et al* 2024 3D printed piezoelectric $BaTiO_3$/Polyhydroxybutyrate nanocomposite scaffolds for bone tissue engineering *Bioengineering* **11** 193

[32] Jacob J, More N, Mounika C, Gondaliya P, Kalia K and Kapusetti G 2019 Smart piezoelectric nanohybrid of Poly(3-hydroxybutyrate- co −3-hydroxyvalerate) and barium titanate for stimulated cartilage regeneration *ACS Appl. Bio Mater.* **2** 4922–31

[33] Ke S, Yang Y, Ren L, Wang Y, Li Y and Huang H 2012 Dielectric behaviors of PHBHHx–$BaTiO_3$ multifunctional composite films *Compos. Sci. Technol.* **72** 370–5

[34] Liu H, Shi Y, Zhu Y, Wu P, Deng Z, Dong Q, Wu M and Cai L 2023 Bioinspired piezoelectric periosteum to augment bone regeneration via synergistic immunomodulation and osteogenesis *ACS Appl. Mater. Interfaces* **15** 12273–93

[35] Jiao H, Song S, Zhao K, Zhang X and Tang Y 2020 Synthesis and properties of porous piezoelectric BT/PHBV composite scaffold *J. Biomater. Sci. Polym. Ed.* **31** 1552–65

[36] Wu P, Chen P, Xu C, Wang Q, Zhang F, Yang K, Jiang W, Feng J and Luo Z 2022 Ultrasound-driven *in vivo* electrical stimulation based on biodegradable piezoelectric nanogenerators for enhancing and monitoring the nerve tissue repair *Nano Energy* **102** 107707

[37] Gorodzha S N *et al* 2017 A comparison study between electrospun polycaprolactone and piezoelectric poly(3-hydroxybutyrate-co-3-hydroxyvalerate) scaffolds for bone tissue engineering *Colloids Surf. B* **160** 48–59

[38] Huang H, Wang K, Liu X, Liu X, Wang J, Suo M, Wang H, Chen S, Chen X and Li Z 2025 Piezoelectric biomaterials for providing electrical stimulation in bone tissue engineering: barium titanate *J. Orthop. Transl.* **51** 94–107

[39] Sheng R *et al* 2023 Fabrication and characterization of piezoelectric polymer composites and cytocompatibility with mesenchymal stem cells *ACS Appl. Mater. Interfaces* **15** 3731–43

[40] Pryadko A S, Mukhortova Y R, Chernozem R V, Shlapakova L E, Wagner D V, Romanyuk K, Gerasimov E Y, Kholkin A, Surmenev R A and Surmeneva M A 2022 Comprehensive study on the reinforcement of electrospun PHB scaffolds with composite magnetic Fe_3O_4—rGO fillers: structure, physico-mechanical properties, and piezoelectric response *ACS Omega* **7** 41392–411

[41] More N, Srivastava A and Kapusetti G 2020 Graphene oxide reinforcement enhances the piezoelectric and mechanical properties of Poly(3-hydroxybutyrate- co −3-hydroxy valerate)-based nanofibrous scaffolds for improved proliferation of chondrocytes and ECM production *ACS Appl. Bio Mater.* **3** 6823–35

[42] Chernozem R V, Surmeneva M A and Surmenev R A 2018 Hybrid biodegradable scaffolds of piezoelectric polyhydroxybutyrate and conductive polyaniline: piezocharge constants and electric potential study *Mater. Lett.* **220** 257–60

[43] Bon S B *et al* 2021 Carbon nanotubes/regenerated silk composite as a three-dimensional printable bio-adhesive ink with self-powering properties *ACS Appl. Mater. Interfaces* **13** 21007–17

[44] European Chemicals Agency (ECHA) 2025 REACH—Registration, Evaluation, authorisation and restriction of chemicals regulation Registered substances factsheets. Substance Infocard (Chloroform) (available at: https://echa.europa.eu/substance-information/-/substanceinfo/100.000.603)

[45] Prat D, Wells A, Hayler J, Sneddon H, McElroy C R, Abou-Shehada S and Dunn P J 2015 CHEM21 selection guide of classical- and less classical-solvents *Green Chem.* **18** 288–96

[46] Gao F, Chang H, Li J, Wang R and Gu Y 2023 Replacing polar aprotic solvents with water in organic synthesis *Curr. Opin. Green Sustain. Chem.* **40** 100774

[47] Mehrpouya M, Vahabi H, Barletta M, Laheurte P and Langlois V 2021 Additive manufacturing of polyhydroxyalkanoates (PHAs) biopolymers: materials, printing techniques, and applications *Mater. Sci. Eng. C* **127** 112216

[48] Grivet-Brancot A, Boffito M and Ciardelli G 2022 Use of polyesters in fused deposition modeling for biomedical applications *Macromol. Biosci.* **22** 2200039

[49] Caputo M R, Fernández M, Aguirresarobe R, Kovalcik A, Sardon H, Candal M V and Müller A J 2023 Influence of FFF process conditions on the thermal, mechanical, and rheological properties of poly(hydroxybutyrate-co-hydroxy hexanoate) *Polymers* **15** 1817

[50] Giubilini A, Messori M, Bondioli F, Minetola P, Iuliano L, Nyström G, Maniura-Weber K, Rottmar M and Siqueira G 2023 3D-Printed Poly(3-hydroxybutyrate- co −3-hydroxyhexanoate)-Cellulose-based scaffolds for biomedical applications *Biomacromolecules* **24** 3961–71

[51] Stanzani V, Giubilini A, Checchi M, Bondioli F, Messori M and Palumbo C 2023 Eco-sustainable approaches in bone tissue engineering: evaluating the angiogenic potential of different Poly(3-Hydroxybutyrate-Co-3-Hydroxyhexanoate)–Nanocellulose composites with the chorioallantoic membrane assay *Adv. Eng. Mater.* **25** 2200934

[52] Pecorini G, Puppi D, Richardson S M, Chen G-Q and Domingos M A N 2025 3D printed poly(3-hydroxybutyrate-co-3-hydroxyexanoate) scaffolds support chondrogenic potential of human primary chondrocytes during *in vitro* culture *Polymer* **320** 128105

[53] Giubilini A, Siqueira G, Clemens F J, Sciancalepore C, Messori M, Nyström G and Bondioli F 2020 3D-printing nanocellulose-Poly(3-hydroxybutyrate- co −3-hydroxyhexanoate) biodegradable composites by fused deposition modeling *ACS Sustain. Chem. Eng.* **8** 10292–302

[54] Ivorra-Martinez J, Quiles-Carrillo L, Boronat T, Torres-Giner S and A. Covas J 2020 Assessment of the mechanical and thermal properties of injection-molded Poly(3-hydroxybutyrate-co-3-hydroxyhexanoate)/Hydroxyapatite nanoparticles parts for use in bone tissue engineering *Polymers* **12** 1389

[55] Şerban D A, Weber G, Marşavina L, Silberschmidt V V and Hufenbach W 2013 Tensile properties of semi-crystalline thermoplastic polymers: effects of temperature and strain rates *Polym. Test* **32** 413–25

[56] Kompelli G, Dauksevicius R, Kleiva A, Turczyn R and Krukiewicz K 2025 3D printable piezoelectric composites manufactured via scalable and sustainable solvent-free multi-extrusion process *Smart Mater. Struct.* **34** 025028

[57] Xie Y, Noda I and Akpalu Y A 2008 Influence of cooling rate on the thermal behavior and solid-state morphologies of polyhydroxyalkanoates *J. Appl. Polym. Sci.* **109** 2259–68

[58] Martinka Maksymiak M, Andrä-Żmuda S, Sikorska W, Janeczek H, Chaber P, Musioł M, Godzierz M, Kowalczuk M and Adamus G 2024 Structural and thermal characterization of bluepha® biopolyesters: insights into molecular architecture and potential applications *Materials* **17** 5863

[59] D'Arienzo L, Acierno S, Patti A and Di Maio L 2024 Cellulose/polyhydroxybutyrate (PHB) composites as a sustainable bio-based feedstock to 3D-printing applications *Materials* **17** 916

[60] Wang Q, Xu Y, Xu P, Yang W, Chen M, Dong W and Ma P 2022 Crystallization of microbial polyhydroxyalkanoates: a review *Int. J. Biol. Macromol.* **209** 330–43

[61] Jin A, Pérez G, Del Valle L J and Puiggalí J 2025 Influence of nucleating agents on the crystallization, thermal, and mechanical properties of Poly(3-hydroxybutyrate-co-3-hydroxyhexanoate) (P3HBHHx) *Appl. Sci.* **15** 6120

[62] Berrabah I, Dehouche N, Kaci M, Bruzaud S, Deguines C H and Delaite C 2022 Morphological, crystallinity and thermal stability characterization of poly(3-hydroxybutyrate-Co-3-hydroxyhexanoate)/zinc oxide nanoparticles bionanocomposites: effect of filler content *Mater. Today: Proc.* **53** 223–7

[63] Sato H, Padermshoke A, Nakamura M, Murakami R, Hirose F, Senda K, Terauchi H, Ekgasit S, Noda I and Ozaki Y 2005 Infrared spectroscopy and x-ray diffraction studies on the structure and thermal behavior of biodegradable polyhydroxyalkanoates *Macromol. Symp.* **220** 123–38

[64] Zhou J, Ma X, Li J and Zhu L 2019 Preparation and characterization of a bionanocomposite from poly (3-hydroxybutyrate-co-3-hydroxyhexanoate) and cellulose nanocrystals *Cellulose* **26** 979–90

[65] Plouzeau M, Belyamani I, Fatyeyeva K, Marais S, Kobzar Y and Cauret L 2023 Recyclability of poly(hydroxybutyrate-co-hydroxyhexanoate) (PHBH) for food packaging applications *Food Packag. Shelf Life* **40** 101170

[66] Renteria A, Diaz J A, He B, Renteria-Marquez I A, Chavez L A, Regis J E, Liu Y, Espalin D, Tseng T-L (Bill) and Lin Y 2019 Particle size influence on material properties of $BaTiO_3$ ceramics fabricated using freeze-form extrusion 3D printing *Mater. Res. Express* **6** 115211

[67] Siviour C R and Jordan J L 2016 High strain rate mechanics of polymers: a review *J. Dyn. Behav. Mater.* **2** 15–32

[68] Liu H, Wu F-Y, Zhong G-J and Li Z-M 2023 Predicting the complex stress-strain curves of polymeric solids by classification-embedded dual neural network *Mater. Des.* **227** 111773

[69] Silva N G S, Zanini N C, Barbosa R F S, de Souza A G, Medeiros S F, Rosa D S and Mulinari D R 2022 A promising sustainable PHB-ZnO composite for development of biodegradable filaments *Polym. Compos.* **43** 144–59

[70] Khieng T K, Debnath S, Ting Chaw Liang E, Anwar M, Pramanik A and Basak A K 2021 A review on mechanical properties of natural fibre reinforced polymer composites under various strain rates *J. Compos. Sci.* **5** 130

[71] Sundar U, Lao Z and Cook-Chennault K 2020 Enhanced dielectric permittivity of optimized surface modified of barium titanate nanocomposites *Polymers* **12** 827

[72] Rocha H, Semprimoschnig C and Nunes J P 2021 Sensors for process and structural health monitoring of aerospace composites: a review *Eng. Struct.* **237** 112231

[73] Xu X, Li J, Ma L and Ma X 2019 Preparation and properties of biocomposite from poly(3-hydroxybutyrate-co-3-hydroxyhexanoate) reinforced with regenerated cellulose *Cellulose* **26** 5427–36

[74] Zhao H, Cui Z, Sun X, Turng L-S and Peng X 2013 Morphology and properties of injection molded solid and microcellular polylactic acid/polyhydroxybutyrate-valerate (PLA/PHBV) blends *Ind. Eng. Chem. Res.* **52** 2569–81

[75] Dani S S, Tripathy A, Alluri N R, Balasubramaniam S and Ramadoss A 2022 A critical review: the impact of electrical poling on the longitudinal piezoelectric strain coefficient *Mater. Adv.* **3** 8886–921

[76] Kannan V, Trassin M and Kochmann D M 2022 Kinetics of ferroelectric switching in poled barium titanate ceramics: effects of electrical cycling rate *Materialia* **25** 101553

[77] Yang Y, Ke S, Ren L, Wang Y, Li Y and Huang H 2012 Dielectric spectroscopy of biodegradable poly(3-hydroxybutyrate-co-3-hydroxyhexanoate) films *Eur. Polym. J.* **48** 79–85

[78] Wu L-P, You M, Wang D, Peng G, Wang Z and Chen G-Q 2013 Fabrication of carbon nanotube

(CNT)/poly(3-hydroxybutyrate-co-3-hydroxyhexanoate) (PHBHHx) nanocomposite films for human mesenchymal stem cell (hMSC) differentiation *Polym. Chem.* **4** 4490

[79] Chilton J A 1995 Electroactive composites *Special Polymers for Electronics and Optoelectronics* (Springer Netherlands) pp 221–55

[80] Stuber V L, Mahon T R, van der Zwaag S and Groen P 2020 The effect of the intrinsic electrical matrix conductivity on the piezoelectric charge constant of piezoelectric composites *Mater. Res. Express* **7** 015703

[81] Ke S, Huang H, Ren L and Wang Y 2009 Nearly constant dielectric loss behavior in poly(3-hydroxybutyrate- co −3-hydroxyvalerate) biodegradable polyester *J. Appl. Phys.* **105** 096103

[82] Nowka M, Ruge K, Schulze L, Hilbig K and Vietor T 2024 Characterization of the anisotropic electrical properties of additively manufactured structures made from electrically conductive composites by material extrusion *Polymers* **16** 2891

[83] Tao R, Shi J, Granier F, Moeini M, Akbarzadeh A and Therriault D 2022 Multi-material fused filament fabrication of flexible 3D piezoelectric nanocomposite lattices for pressure sensing and energy harvesting applications *Appl. Mater. Today* **29** 101596